

1) In the discussion on the difficulties of dealing with aerosols above clouds, the authors seem unaware of recent progress in the development of retrieval approaches to precisely detect and measure aerosols above clouds using POLDER [Waquet et al., 2009], OMI [Torres et al., 2012], and MODIS [Jethva et al., 2013; Meyer et al., 2015]. These three instruments have been in operation for ten years or longer. The authors do not make any mention of these capabilities and any available products from these sensors applicable to their analysis.

We included a discussion on these retrieval approaches in the introduction, since we agree that it is important to mention. We actually have plans to eventually incorporate OMI AOD into our AOD composites in the near future. We added the following sentences...

There has been recent progress on retrieving AOD for absorbing aerosols above clouds from MODIS (Jethva et al., 2013; Meyer et al., 2015) and the Ozone Monitoring Instrument (OMI) (Torres et al., 2012), which could prove very beneficial for tracking the trans-Pacific transport of aerosols. These retrieval techniques take advantage of the highly reflective nature of clouds along with the absorption characteristics of aerosols in the near-UV to visible wavelengths to retrieve AOD when aerosols are lofted above clouds. However, these retrieval techniques rely on a larger number of assumptions than cloud-free aerosol retrievals, which often leads to significant uncertainties of greater than 50% (Jethva et al., 2013; Torres et al., 2012).

2) Much of the trans-Pacific aerosol transport is actually desert dust from sources in the Gobi and Taklamakan deserts. The importance of taking into account the asphericity of desert dust aerosols in remote sensing is well documented. Is this effect properly accounted for in the MODIS and VIIRS algorithms, and in the algorithm developed by the authors for the geostationary IMAGER sensors? If not, why not? Please discuss the rationale.

The MODIS algorithm accounts for nonspherical dust particles as they use T-matrix code to calculate the scattering properties of dust aerosols. Conversely, the VIIRS and GEO algorithms do not account for nonspherical dust particles as these algorithms are based on the 6SV radiative transfer model that uses Mie-scattering calculations. We do not know the actual reasoning for VIIRS using the 6SV and Mie-scattering calculations, but it may be related to the fact that VIIRS is still a relatively new sensor and validation efforts are ongoing. It is very possible that T-Matrix calculations will be used for future releases of the VIIRS AOD algorithm. However, note that preliminary validation efforts showed that AOD from the current VIIRS algorithm compared closely to MODIS AOD (Liu et al., 2014). We do not account for nonspherical dust particles in our GEO algorithms, because these sensors carry only 5 bands which extremely limit their capability in distinguishing between spherical and nonspherical aerosol types in the atmosphere. This is especially true for the GOES imager which cannot utilize the 11-12 μm dust detection test due to missing the 12 μm band. The MTSAT imager is more capable of detecting dust plumes as it carries these 11 and 12 μm bands, but requires larger dust particles in moderate to thick plumes ($\text{AOD} > 0.5$) that are sensitive to these infrared wavelengths (Naeger et al., 2013). Therefore, long-range transport dust events will often be missed by this test. For these reasons, we do not account for nonspherical dust particles in our current GEO algorithms. We have included some discussion on this topic in the manuscript.

When discussing the MODIS AOD algorithm, we added the following sentence...

A noteworthy strength of the MODIS AOD retrieval algorithm is the use of T-Matrix code (Dubovik et al., 2006) to compute scattering properties for non-spherical dust particles, which can lead to significant improvement in characterizing the scattering of dust aerosols and reduce uncertainties in AOD (Dubovik et al., 2002; Levy et al., 2007).

When discussing the VIIRS AOD algorithm, we revised/added the following sentences...

Also, the dust aerosol models over land for these LEO retrievals differ in that the VIIRS dust model is based on Mie-scattering calculations that assume spherical particles while MODIS accounts for non-spherical particles. As a result, we expect VIIRS AOD to encounter higher uncertainties than MODIS when retrieving AOD for dust plumes over land.

When discussing the uncertainties (Section 6), we added the following sentence...

Note that for scenes involving pure dust plumes the RMS errors mentioned above are more representative of lower bound error estimates due to unrealistic dust scattering properties that can arise from the 6SV Mie-scattering calculations, which can lead to higher uncertainties in AOD (Dubovik et al., 2002; Levy et al., 2007).

3) Are the aerosol models used by the MODIS and VIIRS algorithms consistent with each other? The discussion regarding the choice of aerosol models for use in the IMAGER sensor algorithms indicates no effort to make them consistent with the ones used by the LEO sensors. The difference in aerosol model representation can result in non-negligible difference in retrieved aerosol optical depth. Please discuss this issue in the manuscript.

The GEO imager algorithms use identical aerosol models (continental and desert aerosol models) as discussed in Section 3. As mentioned in our response to comment (2), the GEO imagers only carry 5 bands compared to 22 and 36 band onboard VIIRS and MODIS, respectively. The numerous reflectance bands onboard the LEO sensors are used to distinguish between various aerosol types, therefore, these algorithms use a handful of aerosol models and are quite similar. For their ocean aerosol models, the LEO sensors use 9 different aerosol models with nearly identical refractive indices, number median, and standard deviation and effective radius values. The only minor difference between these ocean aerosol models is the slight difference in the band wavelengths. Larger differences exist between the LEO over-land algorithms. Although they both use 5 different aerosol models over-land, they use different values of mean radius, standard deviation of the volume distribution, and refractive indices. Also, the MODIS algorithm uses a nonspherical dust type over land (as mentioned in our response to comment (2)) while VIIRS assumes spherical dust. Therefore, we expect some discrepancies in AOD between MODIS and VIIRS. However, it is important to note that our AOD composite product is centered over the Pacific Ocean where the LEO ocean aerosol models will have the most impact. We have included some discussion in our manuscript along with a comparison between MODIS and VIIRS AOD for a polluted dust plume on 18 March 2014. We included the following in our manuscript...

In Section 2.2, we included...

MODIS AOD is usually retrieved with rather low uncertainties due primarily to the availability of numerous spectral bands. For example, the MODIS team uses seven reflective solar bands to help distinguish between aerosol types in the atmosphere, which has led to the development of a complex aerosol retrieval that uses a total of 14 different aerosol models, nine over ocean and five over land (Levy et al., 2007b). The ocean aerosol models use optical properties representative of four types of water soluble particles, three types of wet sea salt particles, and two types of dust-like particles. Although MODIS over land retrieval only uses five aerosol models (continental, generic, non-absorbing urban-industrial, absorbing smoke, and spheroid dust), they separate between soluble, dust, and soot mode particles for the continental aerosol model, and accumulation and coarse mode particles for the other four models. A noteworthy strength of the MODIS AOD retrieval algorithm is the use of T-Matrix code (Dubovik et al., 2006) to compute scattering properties for the spheroid dust model, which can lead to significant improvement in characterizing the scattering of dust aerosols and reduce uncertainties in AOD (Dubovik et al., 2002; Levy et al., 2007b).

In Section 2.3, we included...

For instance, the VIIRS aerosol retrieval uses the same nine ocean aerosol models as discussed for MODIS. The only minor difference between these ocean aerosol models is the very minimal difference in band wavelengths. Although both VIIRS and MODIS use five different aerosol models over land, they use different values of mean radius, standard deviation of volume distribution, and refractive indices to represent each model. Also, the dust aerosol models over land for these LEO retrievals differ in that the VIIRS dust model is based on Mie-scattering calculations that assume spherical particles while MODIS accounts for non-spherical particles. As a result, we expect VIIRS AOD to encounter higher uncertainties than MODIS when retrieving AOD for dust plumes over land. In addition, there are some significant differences between the VIIRS and MODIS cloud masks and internal screening tests (Jackson et al., 2013). Nevertheless, Liu et al. (2014) conducted an extensive validation of VIIRS AOD against the Maritime Aerosol Network (MAN) where they found that 71% of VIIRS retrievals were within the expected uncertainty range of MODIS retrievals over ocean. Although VIIRS AOD will likely show larger differences when compared to MODIS for scenes of dust aerosols over land, our AOD composite product is centered over the middle of the Pacific Ocean where the LEO ocean aerosol models will be important.

In Section 2.4, we included...

The major disadvantage of these imagers onboard the GOES-15 and MTSAT-2 is that they only have 5 spectral bands, consisting of one visible and four infrared bands (Table 1), compared to the 22 and 36 bands of MODIS and VIIRS. Consequently, these GEO sensors are very limited in their capability to distinguish between various aerosol types in the atmosphere, therefore, we are unable to replicate the complex aerosol retrievals of MODIS and VIIRS. Instead, we develop simplified aerosol retrievals based on only two aerosol

models (continental and desert) as discussed in Section 3.3. Similar to the VIIRS retrieval, the desert aerosol model used in these GEO retrievals assumes spherical particles.

We introduced a new Section 5.4 to show a comparison between the MODIS and VIIRS AOD...

5.4 NRT AOD composites

When generating our AOD composite product, uncertainties may arise from averaging the individual GEO and LEO AOD retrievals onto a common grid (Section 3.6) due to differences in their AOD retrievals, spatial resolution, observation times, and viewing geometry. We expect minimal uncertainties with averaging the GEO AOD onto a common grid, since we developed very similar retrievals algorithms for the GOES and MTSAT imagers that use the same 6SV aerosol model and LUT approaches. In addition, there will only be a small number of instances when both GOES and MTSAT AOD retrievals fall within the same grid box due to the limited overlap between their geographical coverage. Conversely, when averaging the MODIS and VIIRS AOD, significant uncertainties may arise due to the differences between their AOD algorithms as discussed in Section 2.2. Fig. 9a-b shows an example of the MODIS Level 2 AOD retrievals and VIIRS AOD retrievals for the 18 March 2014 case study presented in Section 4.1. The MODIS and VIIRS AOD retrievals are regridded onto identical domains for comparison purposes. These LEO sensors show a very similar spatial distribution of AOD throughout the domain where both retrieve $\text{AOD} > 1$ for the polluted dust plume extending northeast from eastern China ($\sim 33^\circ\text{N}$, 120°E) to the Sea of Japan ($\sim 36^\circ\text{N}$, 135°E) and $\text{AOD} > 0.5$ throughout much of Southeast Asia ($\sim 16^\circ\text{N}$, 100°E). The most significant difference between the LEO AOD retrievals appear over the Korean peninsula ($\sim 38^\circ\text{N}$, 128°E) where MODIS and VIIRS AOD is around 0.7 and 0.5, respectively. Both algorithms utilize their dust models to retrieve AOD in this region, therefore, VIIRS is likely biased low due to the assumption of spherical dust particles in the model. Nevertheless, the correlation between VIIRS and MODIS AOD throughout this entire domain is very high ($R = 0.92$), which suggests that our approach of averaging VIIRS and MODIS AOD to generate the AOD composite leads to a minimal uncertainties.

In the discussion of the GEO observing capabilities, the authors repeatedly refer to GOES or MTSAT reflectances. GOES and MTSAT are the platforms, not the sensors. The actual name of the sensors in both satellites is IMAGER, so please refer to them correctly.

Okay. We corrected all these occurrences.

1
2
3
4
5
6
7
8
9
10
11
12
13
14
15
16
17
18
19
20
21
22
23
24
25
26

**Monitoring and Tracking the Trans-Pacific Transport of Aerosols Using
Multi-Satellite Aerosol Optical Depth Composites**

Aaron R. Naeger¹, Pawan Gupta^{2,3}, and Bradley T. Zavodsky⁴, Kevin M. McGrath⁵

¹University of Alabama in Huntsville, Huntsville, AL, USA

²NASA Goddard Space Flight Center, Greenbelt, MD, USA

³University Space Research Association, MD, USA

⁴NASA Marshall Space Flight Center, Huntsville, AL, USA

⁵Jacobs Engineering Inc., ESSSA Group, Huntsville, AL, USA

Submitted to Atmospheric Measurement Techniques

July 2015

Corresponding Author Address: Aaron R. Naeger, Earth Science System Center, University of Alabama in Huntsville, 320 Sparkman Drive, Huntsville, AL 35805, USA. E-mail: aaron.naeger@nasa.gov

1 **Abstract**

2 The primary goal of this study was to generate a near-real time (NRT) aerosol optical
3 depth (AOD) product capable of providing a comprehensive understanding of the aerosol spatial
4 distribution over the Pacific Ocean, in order to better monitor and track the trans-Pacific
5 transport of aerosols. Therefore, we developed a NRT product that takes advantage of
6 observations from both low-earth orbiting and geostationary satellites. In particular, we utilize
7 AOD products from the Moderate Resolution Imaging Spectroradiometer (MODIS) and Suomi
8 National Polar-orbiting Partnership (NPP) Visible Infrared Imaging Radiometer Suite (VIIRS)
9 satellites. Then, we combine these AOD products with our own retrieval algorithms developed
10 for the NOAA Geostationary Operational Environmental Satellite (GOES-15) and Japan
11 Meteorological Agency (JMA) Multi-functional Transport Satellite (MTSAT-2) to generate a
12 NRT daily AOD composite product. We present examples of the daily AOD composite product
13 for a case study of trans-Pacific transport of Asian pollution and dust aerosols in mid-March
14 2014. Overall, the new product successfully tracks this aerosol plume during its trans-Pacific
15 transport to the west coast of North America as the frequent geostationary observations lead to a
16 greater coverage of cloud-free AOD retrievals equatorward of about 35°N while the polar-
17 orbiting satellites provide a greater coverage of AOD poleward of 35°N. However, we note
18 several areas across the domain of interest from Asia to North America where the GOES-15 and
19 MTSAT-2 retrieval algorithms can introduce significant uncertainties into the new product.

20

21

22

23

24

25

26

27

1 **1. Introduction**

2 Although stricter emission control standards in the United States have led to a reduction
3 in the domestic emissions of particulates since the 1980s, degraded air quality conditions over
4 the western United States have occurred due to foreign dust and pollution aerosols (Yu et al.,
5 2012). For instance, the expanding cities and rapid industrialization of East Asia are major
6 source regions of pollution emissions while biomass burning across Southeast Asia release
7 smoke into the atmosphere (Streets et al., 2003). In addition, frequent dust storms originate from
8 the Taklamakan and Gobi deserts in the late winter and early spring with a daily average dust
9 emission of 1.58 million tons in April (Zhao et al., 2006). These smoke and dust aerosols
10 combine with the other pollutants in a trans-Pacific transport that occurs frequently during late
11 winter and early spring when the East Asian winter monsoon is near its peak strength (Gong et
12 al., 2006). This East Asian winter monsoon brings cold, dry air outbreaks leading to strong
13 surface winds that can efficiently pick up dust from the deserts. Once lofted in the atmosphere,
14 the dust, smoke, and pollution aerosols are quickly transported to the western Pacific by a
15 persistent offshore wind flow from the Asian continent (Talbot et al., 1997). Then, the aerosols
16 are carried by strong mid- to upper-level westerly winds across the Pacific to the western United
17 States where they can be transported from the free troposphere towards the ground. These
18 transported aerosols can reduce the air quality across the United States which can increase the
19 risk of lung cancer and cardiopulmonary mortalities (Pope et al., 2002). Consequently, limiting
20 domestic emissions in the United States alone does not assure that the aerosol effects on human
21 health will be reduced as the total mass of aerosols entering the United States from overseas is
22 similar to that emitted domestically (Yu et al., 2012). Not only can aerosols degrade the air
23 quality, but they can also have direct and indirect radiative effects in the atmosphere through
24 interacting with solar radiation and clouds which can have significant impacts on the climate and
25 weather (e.g., Khain et al., 2005; Ault et al., 2011; Naeger et al., 2013a). Therefore, it is
26 important that we continuously monitor aerosols at a global scale, and determine their
27 concentration and spatial variability, especially during the late winter and early spring period
28 when the trans-Pacific transport of Asian aerosols occurs rather frequently.

29 A major issue when attempting to monitor aerosols across the Pacific is the large amount
30 of cloud cover that often resides over this region. In fact, Mace et al. (2009) used merged data
31 from the Cloud-Aerosol Lidar and Infrared Pathfinder Satellite Observations (CALIPSO) and

1 Cloudsat satellite to show that cloud cover exceeded 90% throughout the North Pacific between
2 July 2006 and June 2007. Aerosol optical depth (AOD) retrievals are generally avoided in
3 cloudy regions due to the difficulty in separating the visible reflectance of the clouds and
4 aerosols that lead to biases in the retrievals. Zhang et al. (2005) found that cloud contamination
5 and cloud brightening lead to an overestimation of 10-20% in the monthly averaged Moderate
6 Resolution Imaging Spectroradiometer (MODIS) AOD over oceans. The MODIS Collection 6.0
7 AOD product has been refined to reduce the cloud contamination issues in Collection 5.1 (Levy
8 et al., 2013). Nonetheless, cloud cover continues to hinder our ability to monitor the trans-
9 Pacific transport of aerosols when using observations from passive (LEO) satellites alone. There
10 has been recent progress on retrieving AOD for absorbing aerosols above clouds from MODIS
11 (Jethva et al., 2013; Meyer et al., 2015) and the Ozone Monitoring Instrument (OMI) (Torres et
12 al., 2012), which could prove very beneficial for tracking the trans-Pacific transport of aerosols.
13 These retrieval techniques take advantage of the highly reflective nature of clouds along with the
14 absorption characteristics of aerosols in the near-UV to visible wavelengths to retrieve AOD
15 when aerosols are lofted above clouds. However, these retrieval techniques rely on a larger
16 number of assumptions than cloud-free aerosol retrievals, which often leads to significant
17 uncertainties of greater than 50% (Jethva et al., 2013; Torres et al., 2012). The CALIPSO
18 satellite carries the active Cloud-Aerosol Lidar and Orthogonal Polarization (CALIOP)
19 instrument that is more equipped for detecting aerosol plumes above cloud layers (Winker et al.,
20 2010). However, the extremely narrow field of view of the vertical curtain-like measurements of
21 CALIOP are of limited value for monitoring the spatial variability of aerosols. Therefore, for
22 this study where we develop a near real time (NRT) AOD composite product for monitoring
23 aerosol plumes across the Pacific Ocean, CALIPSO will only be used to help validate our
24 product.

25 U.S. air quality agencies (e.g., Environmental Protection Agency (EPA)) rely on NRT
26 aerosol products to help provide better forecasts while incorporating the NRT data into their
27 analysis (Al-Saadi et al., 2005). By providing the public with more accurate air quality forecasts,
28 individuals can appropriately adjust their outdoor activities to avoid exposure to poor air quality
29 conditions which can have harmful health impacts. Furthermore, the aerosol indirect effects
30 have recently been incorporated into the Rapid Refresh (RAP) operational model forecast system
31 at the NOAA National Centers for Environmental Prediction (Benjamin et al., 2015). Currently,

1 aerosol fields initialized in the RAP model are based on climatology. Thus, NRT aerosol
2 products can be used to help initialize these operational forecast models with a realistic depiction
3 of the aerosol conditions.

4 In this study, we merge observations from LEO and geostationary (GEO) satellites in
5 order to develop a NRT 6-hourly and daily AOD composite product centered over the Pacific
6 Ocean. The new product will demonstrate the benefits of merging LEO and GEO satellite
7 observations for tracking aerosol plumes in the atmosphere and has the potential to be useful for
8 data assimilation and aerosol forecasting. For instance, the National Aeronautics and Space
9 Administration (NASA) Goddard Earth Observing System version 5 (GEOS-5) model
10 ([Rienecker et al., 2008](#); [Molod et al., 2012](#)) only assimilates aerosol observations from MODIS,
11 but having more frequent satellite observations such as from this study will help model
12 simulation and forecasting of aerosol fields. In the following sections, we discuss the data
13 products used in this study (Section 2), present the methodology for generating NRT AOD
14 composite product (Section 3), show results from a case study of trans-Pacific transport of Asian
15 aerosols (Section 4), discuss uncertainties (Section 5) and validation (Section 6), and conclude
16 with a summary and discussion (Section 6).

18 **2. Data**

19 Table 1 provides a detailed summary of the different satellites and aerosol retrievals used
20 in generating our NRT 6-hourly and daily AOD composite product.

21 **2.1 MODIS**

22 We utilize the MODIS instrument onboard the LEO Aqua and Terra satellites, which has
23 36 spectral bands with center wavelengths between 0.41 and 14.5 μm and spatial resolutions of
24 250 m, 500 m, and 1000 m. In general, the MODIS team retrieves AOD by comparing the
25 reflectances from the solar bands to a lookup table of computed reflectances based on
26 sun/satellite geometry, surface reflectance, and aerosol type (Remer et al., 2005). HAOD
27 products have been under development by the MODIS team with the most recent release of the
28 Collection 6 Level 2 AOD product (Remer et al., 2013). In this study, we use the Collection 5.1
29 Level 2 AOD product, since a NRT version for Collection 6 was not released until early 2016.
30 The Collection 5.1 release of MODIS dark target algorithm provides a 10 km AOD product with
31 uncertainties over ocean and non-bright surfaces of $\pm 0.03 \pm 0.05 * \text{AOD}$ and $\pm 0.05 \pm 0.15 * \text{AOD}$,

1 respectively (Remer et al., 2005; Levy et al., 2010). MODIS AOD is usually retrieved with
2 rather low uncertainties due primarily to the availability of numerous spectral bands. For
3 example, the MODIS team uses seven reflective solar bands to help distinguish between aerosol
4 types in the atmosphere, which has led to the development of a complex aerosol retrieval that
5 uses a total of 14 different aerosol models, nine over ocean and five over land (Levy et al.,
6 2007b). The ocean aerosol models use optical properties representative of four types of water
7 soluble particles, three types of wet sea salt particles, and two types of dust-like particles.
8 Although MODIS over land retrieval only uses five aerosol models (continental, generic, non-
9 absorbing urban-industrial, absorbing smoke, and spheroid dust), they separate between soluble,
10 dust, and soot mode particles for the continental aerosol model, and accumulation and coarse
11 mode particles for the other four models. A noteworthy strength of the MODIS AOD retrieval
12 algorithm is the use of T-Matrix code (Dubovik et al., 2006) to compute scattering properties for
13 the spheroid dust model, which can lead to significant improvement in characterizing the
14 scattering of dust aerosols and reduce uncertainties in AOD (Dubovik et al., 2002; Levy et al.,
15 2007b).

16 The 36 spectral bands of MODIS are also utilized to develop a robust cloud mask that
17 limit cloud contamination from impacting the AOD retrievals. For instance, thin cirrus clouds
18 are difficult to detect and can cause biases in AOD when located above aerosols (Huang et al.,
19 2011), however, the 1.38 μm band onboard MODIS helps mask these clouds and reduce
20 uncertainties in AOD (Ackerman et al., 2006). MODIS also carries the 0.47, 0.66, and 2.12 μm
21 bands that help reduce AOD uncertainties by improving the estimation of surface reflectivity
22 over dark land surfaces, such as vegetation and soils (Levy et al., 2007a). Note that the NRT
23 version of the Collection 5.1 AOD product is distributed with an average latency of
24 approximately 90 minutes via NASA's Land and Atmosphere Near real-time Capability for
25 Earth observing system (LANCE) data system.

26 2.2 VIIRS

27 In addition to MODIS, our NRT product incorporates AOD retrievals from the
28 Visible/Infrared Imager and Radiometer Suite (VIIRS) onboard the Suomi National Polar-
29 orbiting Partnership (NPP) satellite. The VIIRS instrument with its 22 spectral bands was
30 designed to continue the decade-long success of retrieving AOD from MODIS, therefore, the
31 VIIRS AOD retrieval algorithm has similar strengths as just discussed for MODIS. For instance,

1 the VIIRS aerosol retrieval uses the same nine ocean aerosol models as discussed for MODIS.
2 The only minor difference between these ocean aerosol models is the very minimal difference in
3 band wavelengths. Although both VIIRS and MODIS use five different aerosol models over
4 land, they use different values of mean radius, standard deviation of volume distribution, and
5 refractive indices to represent each model. Also, the dust aerosol models over land for these
6 LEO retrievals differ in that the VIIRS dust model is based on Mie-scattering calculations that
7 assume spherical particles while MODIS accounts for non-spherical particles. As a result, we
8 expect VIIRS AOD to encounter higher uncertainties than MODIS when retrieving AOD for
9 dust plumes over land. In addition, there are some significant differences between the VIIRS
10 and MODIS cloud masks and internal screening tests (Jackson et al., 2013). Nevertheless, Liu et
11 al. (2014) conducted an extensive validation of VIIRS AOD against the Maritime Aerosol
12 Network (MAN) where they found that 71% of VIIRS retrievals were within the expected
13 uncertainty range of MODIS retrievals over ocean. Although VIIRS AOD will likely show
14 larger differences when compared to MODIS for scenes of dust aerosols over land, our AOD
15 composite product is centered over the middle of the Pacific Ocean where the LEO ocean aerosol
16 models will be important.

17 Although VIIRS follows the same orbit-track as MODIS Aqua, it is capable of providing
18 additional information on the spatial distribution of AOD due to a wider swath width and higher
19 spatial resolution at swath edge than MODIS (Hillger et al., 2013). VIIRS has a swath width of
20 3000 km versus 2330 km for MODIS and a spatial resolution at swath edge of approximately 1.5
21 km versus 5 km for MODIS. We process AOD data from the VIIRS aerosol EDR via the NOAA
22 Comprehensive Large Array-Data Stewardship System (CLASS) subscription service. However,
23 the VIIRS AOD product via NOAA CLASS has approximately a seven hour latency compared
24 to the 90 minute latency of MODIS AOD via NASA LANCE data system. Consequently, VIIRS
25 retrievals are not incorporated into our 6-hourly composite product as the latency of VIIRS
26 exceeds the time window of the product.

27 2.3 GOES-15 and MTSAT-2

28 Even though the advanced MODIS and VIIRS instruments provide high-quality AOD
29 retrievals, they fly onboard LEO satellites that observe the same location only once per daytime
30 period. Thus, cloud cover can lead to large gaps in the coverage of AOD when only analyzing
31 data from instruments onboard LEO satellites, especially over the generally cloudy Pacific

1 Ocean. To mitigate this issue and more effectively track the trans-Pacific transport of aerosols,
2 we incorporate the high temporal resolution measurements from the NOAA Geostationary
3 Operational Environmental Satellite (GOES-15) and Japan Meteorological Agency (JMA) Multi-
4 functional Transport Satellite (MTSAT-2) geostationary platforms into the NRT AOD composite
5 product. This study uses the northern hemisphere scan modes with a 30 minute temporal
6 resolution for both GOES-15 and MTSAT-2. The high temporal resolution of these GEO
7 sensors can lead to a higher frequency of cloud-free observations than that provided by the LEO
8 sensors, which can help increase the spatial coverage of AOD.

9 The major disadvantage of these imagers onboard the GOES-15 and MTSAT-2 is that
10 they only have 5 spectral bands, consisting of one visible and four infrared bands (Table 2),
11 compared to the 22 and 36 bands of MODIS and VIIRS. Consequently, these GEO sensors are
12 very limited in their capability to distinguish between various aerosol types in the atmosphere,
13 therefore, we are unable to replicate the complex aerosol retrievals of MODIS and VIIRS.
14 Instead, we develop simplified aerosol retrievals based on only two aerosol models (continental
15 and desert) as discussed in Section 3.3. Similar to the VIIRS retrieval, the desert aerosol model
16 used in these GEO retrievals assumes spherical particles. The surface reflectance retrievals
17 (Section 3.2) and cloud masks (Section 3.4) developed for these GEO sensors are also less robust
18 than the LEO sensors due to the lower availability of spectral bands. As a result, AOD retrievals
19 from these GEO satellites will typically have higher uncertainties than those from LEO sensors
20 as shown by the validation study of Paciorek et al. (2008) where the GOES AOD uncertainty
21 range over dark land surfaces was 18-34% with lower values expected over water. Similar
22 uncertainties were associated with a MTSAT AOD retrieval algorithm when validated against
23 ground-based instrumentation at the AEROSOL ROBOTIC NETWORK (AERONET) stations (Kim et
24 al., 2008). Note that easily accessible archives containing AOD data are not available for the
25 GOES-15 and MTSAT-2 satellites, therefore, we develop our own retrieval algorithms for these
26 satellites. The GOES AOD retrieval algorithm developed for this study is similar to the GOES
27 Aerosol/Smoke Product (GASP) discussed in Prados et al. (2008). The latency of our GOES and
28 MTSAT AOD retrievals are typically less than 30 minutes.

29 2.4 AERONET

30 In this study, we use ground-based instrumentation at AERONET stations to assist with
31 developing accurate AOD retrieval algorithms for the GOES and MTSAT satellites. AERONET

1 stations are located throughout the globe, but we focus on 10 of those set across eastern Asia,
2 since aerosols usually propagate over this region prior to their trans-Pacific transport. The sun-
3 sky radiometer instruments at the AERONET stations provide very accurate measurements of
4 aerosol optical properties from the ultraviolet to the near-infrared (Holben et al., 1998). We
5 utilize AOD and single scattering albedo (SSA) data at 500 and 675 nm, then calculate the
6 angstrom exponent by logarithmic interpolation between these wavelengths to derive AOD at
7 550 nm. Reported uncertainties for the Level 2.0 cloud-screened and quality-assured AOD and
8 SSAretrievals are approximately 0.01-0.015 and 0.03-0.07, respectively (Schmid et al., 1999;
9 Dubovik et al., 2000). The interpolation method to derive AOD at 550 nm introduces an
10 additional uncertainty of 0% to 10% (Eck et al., 1999). At the time of this study, Level 2.0 data
11 is not available at a number of AERONET stations across East Asia, therefore, we utilize the
12 Level 1.5 cloud-screened data for these particular stations.

13 2.5 MISR

14 We also utilize AOD retrievals from the Multi-angle Imaging SpectroRadiometer (MISR)
15 onboard EOS Terra satellite to compare against the NRT AOD composite product. The MISR
16 instrument observes the Earth in four spectral bands (0.446, 0.557, 0.671, 0.866 μm) and has
17 nine cameras operating at nine different angles, four in forward, four in backward and one in
18 nadir direction. Its swath width is about 360 km (Diner et al., 2002), and due to the narrow swath
19 width, near global coverage is obtained in 8-9 days at the equator and 2 days near the poles. The
20 relevant MISR data set for this paper is the level 2 aerosol data (MIL2ASAE) containing AOD at
21 4 spectral channels. A detailed description of the aerosol algorithm is given in Kahn et al. (Kahn
22 et al., 2005). MISR AOD over ocean validated using Maritime Aerosol Network (MAN) and
23 found that that MISR AODs are positively biased by about 0.04 with respect to surface measured
24 AODs (Witek et al., 2013). In order to compare against the NRT AOD composite product, the
25 MISR 0.557 μm AOD at 17.6 km spatial resolution have been gridded to $0.5^\circ \times 0.5^\circ$ resolution.

26 2.6 CALIPSO

27 The Cloud-Aerosol Lidar and Infrared Pathfinder Satellite Observations (CALIPSO)
28 carries an active lidar that emits pulses of light at 532 and 1064 nm to produce vertical profiles of
29 the atmosphere (Winker et al., 2003). CALIPSO has the unique ability to measure aerosols
30 above clouds, therefore, we use the level 1B 532 attenuated backscatter profiles to help confirm
31 areas of high AOD among clouds in the AOD composite product. In addition, CALIPSO

1 measures the altitude where aerosols are located in the atmosphere, which we use as an input into
2 the NOAA Hybrid Single Particle Lagrangian Integrated Trajectory Model (HYSPLIT) to
3 forecast the transport path of Asian aerosols. Note that AERONET, MISR, and CALIPSO data
4 are only used to help validate our AOD composite product. In other words, AOD retrievals from
5 these instruments are completely independent of our product.

6

7 **3. Methodology**

8 The schematic flow diagram in Fig. 1 shows the steps involved in generating the NRT
9 AOD composite product. In this section, we discuss each of these steps, but place much of the
10 focus on the four major steps involved in the MTSAT and GOES AOD retrieval algorithms
11 (right side of Fig. 1).

12 **3.1 Clear sky background image**

13 In order to effectively describe the MTSAT and GOES retrieval algorithms, we present
14 an example of how AOD is retrieved for a MTSAT-2 image on 18 March 2014 at 0500 UTC
15 when a polluted dust plume was being transported over the Yellow Sea and Sea of Japan. For
16 the MTSAT-2 imager visible data, we must convert the nominal reflectance (ρ_{nom}) to a calculated
17 reflectance using the monthly linear regression coefficients provided by the Meteorological
18 Satellite Center of JMA. Equation (1) shows how the ρ_{nom} is converted to the calculated or
19 satellite reflectance (ρ_{sat}) where C_0 and C_1 are the intercept and slope linear regression
20 coefficients, d is the Earth-Sun distance in astronomical units, and θ_0 is the solar zenith angle.
21 The linear regression coefficients for March 2014 are 1.2257 and -0.0006 for C_0 and C_1 ,

$$\rho_{sat} = \frac{(C_0 + C_1 * \rho_{nom}) * d^2}{\cos(\theta_0)} \quad (1)$$

22 respectively. The first step of the MTSAT AOD retrieval algorithm is to gather visible imagery
23 data at 0500 UTC beginning 19 February through 18 March (28 total) and calculate ρ_{sat} . Then,
24 we find the second lowest ρ_{sat} for each pixel during the 28 day period, which generates the clear-
25 sky background (ρ_{min}) image. The same approach is taken to generate the ρ_{min} for the GOES-15
26 imager except that the ρ_{sat} is calculated based on calibration coefficients provided by the NOAA
27 NESDIS Center for Satellite Applications and Research (STAR). Note that we chose the 28 day
28 period after conducting sensitivity tests using 21, 24, 28, and 35 day periods, which is discussed
29 in Section 5. Although our sensitivity tests indicated that 28 days is the optimal period, the

1 variation in solar geometry throughout the four week period can still lead to considerable
2 uncertainties, especially at lower surface reflectances.

3 3.2 Surface reflectance (R_{sfc}) retrieval

4 For the second step, we retrieve the surface reflectance (R_{sfc}) by removing the
5 atmospheric effects from the ρ_{min} image via a look-up table (LUT_{sfc}). The LUT_{sfc} is generated
6 using the Version 1.1 of the Second Simulation of a Satellite Signal in the Solar Spectrum Vector
7 (6SV) radiative transfer model (RTM) (Kotchenova et al., 2006; Kotchenova and Vermote,
8 2007)6SV code. The highly accurate 6SV code contains the same atmospheric correction
9 procedure used by the MODIS team (Vermote and Kotchenova, 2008). However, in developing
10 the LUT_{sfc} , we are required to make some assumptions regarding the state of the atmosphere
11 throughout the ρ_{min} image. First, in order to remove the atmospheric effects, we used
12 temperature, water vapor, and ozone information from the U.S. standard profiles already
13 available in the 6SV code. Our sensitivity tests in Section 5.1 show that using U.S. standard
14 profiles cause uncertainties in AOD of less than 1%, which agrees with the findings of Levy et
15 al. (2013). Second, we assume a background AOD of 0.05 since the visible bands onboard the
16 MTSAT-2 and GOES-15 satellites have been shown to be insensitive to low concentrations of
17 AOD (Knapp et al., 2005). After making these assumptions, the 6SV code is used to simulate
18 the top of atmosphere reflectance (ρ_{toa}) values for a range of 16 θ_0 , 16 viewing zenith angles (θ),
19 15 ϕ , and 8 R_{sfc} (i.e., LUT_{sfc}). We search the LUT_{sfc} for the solar/satellite geometry that most
20 closely matches that for each pixel in the MTSAT-2 and GOES-15 imager scan. After
21 identifying the solar/satellite geometry match, we retrieve the R_{sfc} for each pixel by interpolating
22 ρ_{min} to the simulated ρ_{toa} values. Fig. 2a displays the MTSAT-2 imager ρ_{sat} on 18 March 2014,
23 where a plume of dust and pollution extending from China to over the Sea of Japan trails behind
24 a frontal band associated with a low-pressure system near Japan. The R_{sfc} retrievals for each
25 pixel in the MTSAT-2 imager scan are shown in Fig. 2b where we only retrieve the R_{sfc} when the
26 θ_0 and θ is less than 70° as AOD retrievals at larger angles are associated with significant
27 uncertainty (e.g., Ignatov and Stowe, 2002). Also, AOD is not retrieved for the pixels
28 highlighted in red ($R_{sfc} > 35\%$), since they are likely contaminated with either cloud, snow, or
29 ice. However, we are able to attempt an AOD retrieval for the majority of the pixels in the R_{sfc}
30 image as most of the scene appears to be uncontaminated.

31 3.3 AOD retrieval

1 The third step consists of retrieving the GOES and MTSAT AOD via additional LUTs ,
2 which are created similar to LUT_{sfc} except that we use the 6SV code to simulate the ρ_{toa} for 7
3 different AODs in addition to the range of θ_0 , θ , φ , and R_{sfc} used in creating LUT_{sfc} . The most
4 significant assumption in creating these LUTs is the selection of the aerosol model as the
5 simulated ρ_{toa} can vary greatly based on the optical properties of the aerosols. Thus, prior to
6 selecting an aerosol model for our domain, we conduct a detailed comparison between the
7 observed ρ_{sat} and simulated ρ_{toa} using seven different 6SV aerosol models for 24 unique cases
8 occurring over AERONET stations across eastern Asia during March and April 2014. Overall,
9 this comparison showed that selecting the 6SV continental and desert aerosol models would
10 introduce the least amount of uncertainty compared to the other aerosol models available in the
11 code, which is discussed in Section 5.3. Therefore, to represent these aerosol models we create
12 two separate LUTs for retrieving AOD, LUT_{cont} and LUT_{dust} . We retrieve AOD based on these
13 LUTs by using the R_{sfc} from the surface reflectance retrieval step and then interpolating ρ_{sat} to the
14 simulated ρ_{toa} values to retrieve the AOD. Note that we do not invoke the LUT_{dust} unless a pixel
15 passes a handful of dust detection techniques that are explained in Section 3.4. Also, separate
16 LUTs were generated for the visible bands of the MTSAT-2 and GOES-15 imagers due to
17 having unique spectral response functions. The spectral response functions for the visible bands
18 onboard these satellites were not available in the 6SV1.1 RTM, therefore, we updated the 6SV
19 source code to account for these bands prior to producing the LUTs.

20 3.4 Cloud and dust detection

21 For the fourth and final step of the MTSAT and GOES retrieval algorithms, we use cloud
22 and dust detection procedures to disregard contaminated AOD retrievals and identify any pixels
23 influenced by dust. Developing accurate cloud detection algorithms for these GEO satellites is
24 not a trivial step due to their lower spatial resolution and limited number of spectral bands. In an
25 effort to obtain as much information as possible from 4 spectral bands (6.7 μm water vapor band
26 is not used), we extract reflectance and temperature from the 3.9 μm band based on Mecikalski
27 et al. (2010). Then, we use spectral, spatial, and temporal techniques based on the reflectance
28 and temperature information from the 4 spectral bands to identify clouds and dust in each
29 satellite image. The cloud/dust detection techniques for these satellites are similar even though
30 the GOES imager has a 13.3 μm band instead of the 12.0 μm band onboard MTSAT. However,
31 we were able to develop more sophisticated dust detection techniques for MTSAT as dust

1 particles have a larger imaginary index of refraction at 10.8 μm compared to 12.0 μm while most
2 other aerosol and cloud types have an opposite trend (Ackerman, 1997). This can influence a
3 negative difference between the 10.8 and 12.0 μm bands, which can be used to identify dust
4 aerosols (Sokolik, 2002; Naeger et al., 2013b). In this paper, we will only briefly step through
5 the MTSAT cloud/dust detection procedure (Table 3), but will note any important differences
6 that arise in the GOES procedure. The techniques shown in Table 3 were developed after close
7 examination of dozens of MTSAT satellite images involving cloud and aerosols throughout the
8 year 2014. Thus, this procedure can be applied during any season, but note that it will generally
9 overestimate cloud coverage as its main purpose is to limit sub pixel cloud contamination and
10 cloud adjacency effects from impacting the AOD retrievals. The spatial techniques help greatly
11 with disregarding AOD retrievals impacted by these cloud effects over both land and ocean, but
12 they work especially well over the homogeneous ocean surface where the thresholds for cloud
13 detection were able to be set to lower values. Note that we also detect and screen out all possible
14 sunglint affected pixels during this step.

15 Fig. 2c shows the overall results of the cloud/dust procedure for θ_0 and $\theta < 75^\circ$ on 18
16 March 2014 at 0500 UTC. We run the procedure in the same order as shown in Table 3. After
17 passing one of the spectral, spatial, or temporal techniques, the pixel is immediately labeled as
18 cloud using the corresponding number in the right-hand column. A pixel must fail all the cloud
19 detection techniques to be labeled cloud-free. We only retain AOD retrievals that are associated
20 with cloud-free pixels. Approximately 80% of the valid MTSAT pixels are labeled as cloud and
21 the spectral techniques detect about 71% of these clouds. Spectral technique #3 does not appear
22 in the GOES cloud/dust procedure due to the absence of the 12.0 μm band. The spatial
23 techniques detect a significant fraction of the remaining clouds (~28%), especially in regions of
24 scattered cumulus clouds over the ocean. Although the impact of the temporal techniques
25 appears very minimal in Fig. 2c, they are able to detect some lingering clouds (e.g., $\sim 40^\circ\text{N}$,
26 120°E) that could lead to artifacts in the NRT AOD composite product.

27 Since possible dust regions can be mislabeled as cloud by our procedure due to their
28 similar spectral characteristics, we use four dust techniques to locate pixels mislabeled as cloud
29 and relabel them as cloud-free. The special techniques were developed based on the fact that
30 dust regions can have strong positive 3.8-10.8 μm values similar to clouds, but are often more
31 homogeneous than clouds while influencing 10.8-12.0 μm values less than -1 K. A considerable

1 number of pixels are relabeled as cloud-free in northern China. The final dust technique in Table
2 3 operates only on cloud-free pixels. If a pixel passes this technique, then the AOD is revised
3 based on the LUT_{dust} instead of the LUT_{cont} that was assumed for each pixel during the third step.
4 Although similar to MTSAT, the GOES dust detection technique is not as robust as the 10.8-12.0
5 μm test cannot be included in the GOES technique due to the absence of the 12.0 μm band.
6 After applying the cloud/dust detection procedure, we arrive at our final cloud-cleared AOD map
7 for this MTSAT imager scan at 0500 UTC on 18 March (Fig. 2d). The map shows high AOD >
8 1.0 associated with the thick pollution and dust plume propagating from eastern Asian to over the
9 Pacific Ocean. Pollution and smoke plumes are also causing high AOD in regions across
10 southern Asia. Thus, we are able to depict some features on this AOD map, but the large gaps in
11 coverage due to clouds make it difficult to fully understand the spatial distribution of aerosols.

12 3.5 LEO AOD products

13 While retrieving AOD from the GEO imager data, we also process the Aqua and Terra
14 MODIS AOD via the NASA LANCE data system and VIIRS AOD via the NOAA CLASS
15 service (left side of Fig. 1). To help prevent poor quality MODIS AOD from being introduced
16 into our AOD composite maps we use the MODIS cloud fraction parameter and quality
17 assurance flags to ignore retrievals associated with marginal confidence and cloud cover > 70%.
18 We disregard poor quality VIIRS AOD by using the quality flags to ignore retrievals where at
19 least one pixel among the 8x8 pixel region cloud or cirrus contaminated.

20 3.6 NRT AOD composites

21 In order to generate the NRT AOD composites, we use all the valid GEO and LEO AOD
22 data that was processed over a 24 hour period beginning 1200 UTC each day. At the end of the
23 24 hour AOD composite period, AOD from the GEO and LEO sensors are regridded and
24 averaged onto a common domain with $0.5^\circ \times 0.5^\circ$ spatial resolution centered over the central
25 Pacific Ocean in order to effectively track the trans-Pacific transport of aerosols. The rather
26 coarse $0.5^\circ \times 0.5^\circ$ grid is suitable for our particular application where larger scale, more
27 homogeneous aerosol plumes are the focus. We use a nearest neighbor approach to find and
28 calculate the average of all AOD retrievals for each GEO imager that fall within each grid box.
29 This same operation is performed for the LEO AOD retrievals. Uncertainties with the averaging
30 the GEO and LEO AOD onto the same grid are discussed in Section 6. These GEO and LEO
31 AOD composite maps are then merged together to generate the final daily AOD composite maps.

1 When merging these composite maps, the LEO AOD is chosen to represent a grid box when both
2 LEO and GEO AOD are available due to the higher uncertainty associated with the GEO
3 retrievals.

4 In our current methodology, we do not apply techniques to account for the differences in
5 observation times or spatial resolutions between the GEO and LEO sensors, which may lead to
6 undesirable jumps in AOD when merging the different sensors on a common grid. However,
7 according to the case in Section 4, our simplified approach does not lead to frequent AOD jumps
8 in our daily composite product. We plan to develop more advanced methodologies in the future
9 for merging AOD information from the next-generation NOAA GOES-R and recently launched
10 JMA Himawari satellites. Our primary goal here is to develop and evaluate a simple
11 methodology that shows the application of merging AOD from current GEO and LEO satellite
12 sensors.

13

14 **4. Results**

15 4.1 18 March 2014

16 The top three panels in Fig. 3 display the daily AOD composites for the case study on 18
17 March 2014. The central time of the AOD composite product is 0000 UTC, since we used
18 satellite information between 1200 UTC on 17 March and 1200 UTC on 18 March to generate
19 the product. Fig. 3a is an example of the daily AOD composite with only MTSAT/GOES
20 retrievals while Fig. 3b is an example with only MODIS/VIIRS retrievals. All these satellite
21 retrievals are combined onto the same map to generate the final version of the daily AOD
22 composite product, which shows a more complete picture of the spatial distribution of aerosols
23 during this 24 hour period (Fig. 3c). A massive aerosol plume extends from eastern China to
24 almost the central Pacific region as moderate AOD of approximately 0.6 is identified around
25 38°N 165°E. Some moderate to thick aerosols are still propagating from the central China
26 region behind the extensive cloud feature in the MTSAT 0.68 μm image suggesting that poor air
27 quality and visibility may plague eastern China in the short-term. A fairly extensive aerosol
28 plume is moving from southeast China to the tropical Pacific around 20°N 120°E while aerosol
29 layers with AOD > 0.5 are impacting much of Southeast Asia (~15°N, 100°E). It is important to
30 note that the MTSAT/GOES retrievals blend into Fig. 3c rather well due to the overall good
31 agreement in the spatial patterns of AOD between Fig. 3a and b. For example, the aerosol plume

1 moving from Southeast China to the tropical Pacific is not fully represented using
2 MODIS/VIIRS AOD retrievals alone. Fortunately, the MTSAT retrievals fill this region with
3 AOD that blends in very well with the surrounding MODIS/VIIRS AOD. Also, the massive
4 aerosol plume from eastern China is more fully represented in Fig. 3c than in Fig. 3b, since
5 MTSAT is able to observe additional cloud-free regions among the plume.

6 Although the spatial patterns of AOD compare fairly well between Fig. 3a and b, some
7 important differences exist between the maps. The MTSAT/GOES AOD map fails to represent
8 the region of moderate AOD identified in the MODIS/VIIRS map around 38°N 165°E. This
9 region is nearly outside the viewing range of GOES but well within the viewing range of
10 MTSAT. However, MTSAT is unable to find a cloud-free pixel among this region of broken
11 clouds (Fig. 2a) due to its relatively coarse spatial resolution of 5 km at nadir. The much finer
12 spatial resolution of the MODIS (~0.5 km at nadir) and VIIRS visible channels (~0.74 km at
13 nadir) compared to the GEO sensors allows retrievals to be performed in these cloud-free
14 regions. Furthermore, MTSAT/GOES has a high bias in AOD of 0.02 compared to
15 MODIS/VIIRS when comparing the average of all AOD retrievals poleward of 30°N while a low
16 bias of the same magnitude exists for AOD retrievals equatorward of 30°N. However, regions of
17 larger discrepancies are apparent when comparing Fig. 3a and b. For instance, MTSAT AOD is
18 about 0.2 lower than MODIS/VIIRS around 30°N 137°E. The MODIS/VIIRS AOD in this area
19 is generally within ± 0.05 of the MISR AOD (Fig. 3e) while MTSAT is lower than MISR by -
20 0.05 to -0.20 (Fig. 3d). The closer agreement between MISR and MODIS/VIIRS AOD suggests
21 that the LEO retrievals are more accurate than MTSAT. Note that MISR retrievals are strictly
22 for intercomparison purposes and completely independent of the AOD composite product. This
23 tendency of MTSAT/GOES to be biased low is primarily caused by cloud cover influencing the
24 ρ_{min} image which then leads to overestimations in the R_{sfc} retrievals (Fig. 2b). Clouds tend to
25 impact the R_{sfc} retrievals more often in the north and central Pacific as the MTSAT/GOES spatial
26 resolution decreases. On the other hand, the high bias over the tropical Pacific is mostly due to
27 cloud contamination influencing the MTSAT AOD retrievals, which is evident by the areas of
28 $AOD > 1.0$ appearing over parts of the tropical western Pacific (~2°N, 115°W). Neither
29 MODIS/VIIRS or MISR depict these same areas of $AOD > 1.0$. There are large discrepancies
30 between AOD retrievals across portions of Southeast Asia as indicated by the MISR overpass
31 around 15°N 107°E. MODIS/VIIRS AOD is generally between 0.5 and 0.7 in this region while

1 MTSAT AOD reaches 1.0 in some locations. MISR AOD is considerably lower with values of
2 around 0.3. These large differences in AOD across the region make it very difficult to assess the
3 MTSAT retrievals using these passive sensors alone. The highly uncertain AOD retrievals can
4 be attributed to the complex terrain of Southeast Asia along with the scattered cloud coverage on
5 this day. Fortunately, it is very unlikely that any aerosol plumes originating from this region will
6 undergo trans-Pacific transport.

7 The CALIPSO made several transects directly over the aerosol plumes across the western
8 Pacific and eastern Asia on 18 March. We analyze the CALIPSO transects indicated in Fig. 3c
9 (black lines) from east to west. Fig. 4a shows the 532 nm attenuated backscatter profiles from
10 about 0320 UTC on 18 March where moderate backscatter values are measured from an aerosol
11 plume at approximately 3 km in height (box 1). The CALIPSO Vertical Feature Mask (VFM)
12 and aerosol subtype browse images confirmed this region of moderate backscatter as aerosol
13 consisting of dust and polluted dust. This aerosol layer is likely interacting with the high, thick
14 clouds to the north in Fig. 4a. The daily AOD composite product (Fig. 3c) reveals moderate to
15 high AOD in the vicinity of this aerosol layer. Several noteworthy aerosol plumes are measured
16 by CALIPSO during the transect at about 0500 UTC (Fig. 4b). First, moderate backscatter
17 values are associated with an aerosol layer from about 18-24°N (box 2). Even though the
18 CALIPSO transect shows scattered low clouds residing beneath much of the aerosol layer, the
19 AOD composite is still able to depict AOD ranging from 0.3 to 0.7 in this same area. Second,
20 CALIPSO measures very strong backscatter signals from the aerosol region in box 3, which is
21 clearly shown in the composite product by the large area of $AOD > 1$. The CALIPSO aerosol
22 subtype algorithm labels this aerosol region as a mixture of dust and polluted dust. Lastly,
23 CALIPSO measures moderate backscatter from a fairly thin aerosol plume mixed with smoke
24 and polluted dust in box 4. A close inspection of the AOD composite reveals a confined area of
25 $AOD \sim 0.3$ in the vicinity of the aerosol plume. A couple hours later at about 0640 UTC
26 CALIPSO flew directly over the very complicated scene of Southeast Asia (Fig. 4c) consisting
27 of clouds located within an aerosol layer (box 5) and then aerosols above terrain features (box 6).
28 The CALIPSO VFM image revealed that portions of the aerosol layer in box 5 were cloud-free,
29 particularly near 10°N. CALIPSO measures moderate to high backscatter in these cloud-free
30 regions, which suggests that the $AOD > 0.5$ shown in the AOD composite represents the aerosol
31 layers across this region rather well. Thus, it is very likely that MISR is severely

1 underestimating the AOD in this region while the MODIS/VIIRS and MTSAT AOD retrievals
2 are performing much better. Lower backscatter is measured by CALIPSO over the terrain
3 features in box 6, and the AOD composite shows lower AOD ranging from 0.4 to 0.5 in this
4 same area. Overall, the CALIPSO transects indicate our AOD composite realistically represents
5 the intensity of the aerosol plumes throughout western Pacific and Asia.

6 7 4.2 HYSPLIT trajectory analysis

8 We investigate the transport pathways for three of the aerosol plumes identified in the
9 CALIPSO 532 nm attenuated backscatter profiles (boxes 1, 2, and 5) through the online
10 HYSPLIT tool from NOAA Air Resources (<http://ready.arl.noaa.gov/HYSPLIT.php>) (Rolph,
11 2016) to calculate the forward trajectories of air parcels. Note that these trajectory calculations
12 do not account for aerosol particulate transport and wet and dry deposition, which can influence
13 aerosol pathways, especially during long-range transport events. We run HYSPLIT for an
14 ensemble of 27 trajectories from each aerosol plume location for a 96 hour period beginning at
15 0500 UTC on 18 March until that same time on 22 March using National Centers for
16 Environmental Prediction (NCEP) reanalysis meteorological data. The CALIPSO attenuated
17 backscatter profiles are used to estimate the altitude of the three aerosol plumes, which are all
18 around 3 km. The start altitude of the trajectory simulations is a necessary input that must be
19 given to the NOAA HYSPLIT model when making these simulations. Fig. 5 shows that nearly
20 all the HYSPLIT trajectories initialized from position 1 (box 1) propagate the polluted dust
21 plume to over the far eastern extent of the Pacific Ocean or over the Pacific Northwest by 22
22 March at 0500 UTC. This dust/pollution plume is an excellent example of a typical trans-Pacific
23 transport pathway via the midlatitude westerly winds (Wilkening et al., 2000). The ensemble of
24 trajectories initialized from position 2 (box 2) suggest the aerosol plume is likely to move
25 westward. A handful of trajectories show the plume moving slowly eastward, but they never
26 make any significant headway toward North America by the end of the 4 day period. All the
27 trajectories initialized from position 5 (box 5) located over Southeast Asia took the aerosol
28 plume south and west of the initial position. Consequently, the possible discrepancies in AOD
29 that can appear over Southeast Asia are not considered a significant problem when using the
30 AOD composites to track the trans-Pacific transport of aerosols.

1 4.3 23 March 2014

2 To confirm whether this polluted dust plume reached the western coast of North America
3 we generated the daily AOD composite with a central time of 0000 UTC on 23 March shown in
4 Fig. 6c. The daily AOD composite depicts moderate AOD of 0.4 to 0.5 over the extreme eastern
5 Pacific, which suggests that remnants of the plume in the western Pacific experienced trans-
6 Pacific transport. However, the majority of the HYSPLIT ensemble runs predict the aerosol
7 plume to be further east than shown in the AOD composite with a handful of runs showing the
8 plume over western North America by 22 March at 0500 UTC. These differences in aerosol
9 plume location between the HYSPLIT runs and the AOD composite are likely attributed to the
10 fact the model does not account for long-range aerosol transport processes. This case study
11 shows the utility of the AOD composites for model validation and the potential benefit of using
12 the composites for model assimilation.

13 The overall results of the panels in Fig. 6 are similar to that shown for the 18 March case.
14 Again, the MTSAT/GOES retrievals in Fig. 6a blend nicely into the MODIS/VIIRS AOD map in
15 Fig. 6b to generate a more robust spatial distribution of aerosols. Many of the same features are
16 revealed on the MTSAT/GOES and MODIS/VIIRS AOD maps, such as the dense aerosol plume
17 over eastern Asia. However, the MTSAT/GOES AOD map also reveals areas of optically
18 thicker aerosol over northern China (~40°N, 106°E) that are not indicated on the MODIS/VIIRS
19 map. CALIPSO measured a fairly large region of moderate backscatter from dust aerosols
20 during a nighttime transect over this same region in northern China on 23 March at about 1900
21 UTC (not shown), which suggests that MTSAT is realistically representing the AOD over this
22 region. Over the extreme eastern Pacific, GOES retrieves moderate AOD for the transported
23 polluted dust plume, but MODIS/VIIRS is able to retrieve a larger region of AOD associated
24 with this plume due to their significantly higher spatial resolution in these northerly locations.
25 MTSAT/GOES retrievals appear to encountering issues in similar areas as shown for the 18
26 March case. For instance, the MTSAT/GOES AOD retrievals are biased high compared to
27 MODIS/VIIRS across the tropical Pacific, especially in the latitude band from 10-20°N over the
28 eastern Pacific. However, some of the areas of elevated AOD around 0.3 depicted in the
29 MTSAT/GOES map correspond well to that shown in the MODIS/VIIRS map (e.g., ~15°N,
30 165°W). MTSAT AOD is significantly lower than MODIS/VIIRS along the coast of southeast
31 China (~25°N, 115°E) due to persistent cloud cover in this area throughout the 28 day period

1 used to retrieve R_{sfc} . Large discrepancies between MTSAT and MODIS/VIIRS AOD are once
2 again appearing in areas throughout Southeast Asia and eastern India.

3 To quantitatively show the gain in spatial coverage due to the inclusion of the GEO
4 sensors in our daily AOD composite maps we calculate the number of valid AOD retrievals
5 along with the percent coverage of those retrievals based on the total number of available grid
6 boxes (70400 grid boxes) across our composite domain. These statistics are calculated for the
7 daily AOD composite maps when only LEO (MODIS/VIIRS) and GEO (MTSAT/GOES)
8 sensors are considered and when both LEO and GEO sensors are considered in developing our
9 final product. We show statistics for a six day period, which includes the 18 and 23 March case
10 studies presented in this paper (Table 4). Overall, the LEO sensors provide more spatial
11 coverage compared to the GEO sensors (67% versus 60%) during this six day period. As shown
12 in this paper, the higher percentage for the LEO sensors is partly due to the fact that they have
13 better coverage throughout the northern regions of the AOD composite domain. The LEO
14 sensors also have better coverage over the central Pacific and over the far eastern and western
15 portions of the composite domain, which is due to the limited geographical coverage of the GEO
16 sensors. The GEO retrieval algorithms developed in this study further limit their geographical
17 coverage by restricting θ to less than 70° to avoid the very large uncertainties that arise at these
18 oblique angles. Although the LEO coverage is better than GEO, introducing the GEO sensors
19 into the AOD composite maps still leads to considerable increases in spatial coverage for our
20 final product. For the six day period in Table 4, the inclusion of the GEO sensors improves the
21 spatial coverage of AOD from 67% for the LEO sensors to 81% for our merged LEO/GEO
22 product. The GEO sensors lead to an improvement in the spatial coverage of AOD as their high
23 temporal resolution allows for the identification of more cloud-free regions where a valid AOD
24 can be retrieved.

25

26 **5. Uncertainties**

27 5.1 Atmospheric profiles

28 To understand the uncertainty with using temperature, water vapor, and ozone
29 information from U.S. standard profiles in the AOD retrieval procedure, we conducted a
30 sensitivity analysis where atmospheric profiles from $0.5 \times 0.5^\circ$ Global Forecast System (GFS)
31 data were input into the 6SV model. We extracted the GFS profiles from locations that represent

1 tropical, midlatitude, and subarctic conditions during January and July 2014, and used different
2 θ_0 , θ , and R_{sfc} for each location to assess their impact on the uncertainty (Table 5). Fig. 7a shows
3 compares several of these GFS profiles against the U.S. standard profile to show that vastly
4 different atmospheric conditions are being input into the 6SV. For this sensitivity analysis, we
5 first run the 6SV in atmospheric correction mode to retrieve ρ_{min} for each profile, which is then
6 used to retrieve ρ_{toa} . Note we perform this analysis on MTSAT-2, since its spectral response
7 function extends to slightly larger wavelengths compared to GOES-15 where water vapor
8 absorption has a stronger impact. Overall, ρ_{toa} is very similar between the U.S. standard and
9 GFS profiles in each region (Fig. 8b), which proves that the standard profile is causing only a
10 minimal amount of uncertainty in the AOD retrieval procedure. The uncertainty is slightly
11 higher over subarctic locations due mostly to the much drier conditions than that in the U.S.
12 standard profile, but errors are still less than 1% for an AOD of 3.

13 5.2 Surface reflectance (R_{sfc}) retrieval

14 A significant source of uncertainty in our study is associated with the R_{sfc} retrievals due to
15 the variation in solar geometry throughout the 28 day period. Overall, we found that the
16 uncertainty in AOD increases with decreasing R_{sfc} values. For instance, the AOD uncertainty
17 can be as high as 17% at R_{sfc} values of 10% but increase to almost 34% at R_{sfc} values of 5%.
18 Note that these values represent the maximum possible uncertainty that can be associated with a
19 cloud-free R_{sfc} retrieval. Nevertheless, this uncertainty is the most likely explanation for the
20 MTSAT/GOES AOD bias found over portions of the Pacific Ocean on 18 and 23 March. When
21 attempting to use a 21 and 24 day period for the R_{sfc} retrievals, we noticed major issues with
22 cloud contamination that led to significant underestimations in AOD.

23 5.3 Aerosol models

24 The most significant assumption in creating the LUTs in our GEO AOD retrieval
25 algorithms is the selection of the aerosol model as the simulated ρ_{toa} can vary greatly based on
26 the optical properties of the aerosols. In order to select the 6SV aerosol models that would
27 introduce the least amount of uncertainty in our retrieval algorithms, we conducted a detailed
28 comparison between the observed ρ_{sat} and simulated ρ_{toa} using seven different 6SV aerosol
29 models for 24 unique cases occurring over AERONET stations across eastern Asia during March
30 and April 2014. For each case, we provide the 6SV with the R_{sfc} retrieval value closest to the
31 AERONET station along with precise values of θ_0 , θ , and φ from the MTSAT-2 imager, and

1 AERONET 550 nm AOD. Then, we simulate the 6SV using these identical input values and
2 compare the ρ_{toa} values to the MTSAT-2 imager ρ_{sat} in order to determine the aerosol model with
3 the least amount of uncertainty. Fig. 8 presents the results from each aerosol model for the 24
4 cases where the continental model (red) simulated the most realistic ρ_{toa} values as ρ_{sat} was
5 slightly overestimated at values less than about 16% and underestimated at values greater than
6 about 20%. The average difference between ρ_{sat} and ρ_{toa} for the 24 cases was only -0.09% when
7 using the continental aerosol model leading to the lowest root mean square (RMS) error of
8 1.31% (Table 6). SSA retrievals from the AERONET stations across eastern Asia were often
9 around 0.90 at 500 nm with a decreasing trend at larger wavelengths, which is nearly identical to
10 the prescribed SSA of the continental model. Although pollution events are observed frequently
11 over eastern Asia, we were surprised by such excellent agreement between AERONET stations
12 and the continental aerosol model due to the fact that dust emitted from the Taklamakan and
13 Gobi deserts is often transported over eastern Asia, especially in the early spring which is the
14 focus of our study. This suggests that pure dust plumes, which are generally associated with
15 SSA values of around 0.95 (Seinfeld et al., 2004; Hsu et al., 2006), often undergo modification to
16 a polluted dust mixture with lower SSA values after being transported over the polluted region of
17 eastern Asia. In fact, during the polluted dust case on 18 March 2014 (i.e., Fig. 2), SSA from the
18 XiangHe AERONET site were around 0.89.

19 We found a couple dust plumes nearby their source region in the Taklamakan desert on
20 25 and 29 April 2014. The Taklamakan AERONET site retrieved SSA values from 0.93 to 0.95
21 for these pure dust plumes, which are comparable to that found for dust during the Asian Pacific
22 Regional Aerosol Characterization Experiment (ACE-Asia) from 30 March to 3 May 2001.
23 Therefore, to better represent the dust optical properties we also incorporated the desert aerosol
24 model into our AOD retrieval algorithm, which uses a more appropriate SSA at 500 nm of about
25 0.95 that increases with larger wavelengths. Overall, for the instances when our AOD retrieval
26 algorithm correctly identifies polluted and pure dust events, Table 6 suggests that RMS errors
27 will be minimal (~1.3%). These errors can increase to about 3.8% for the instances when our
28 algorithm incorrectly identifies pollution as dust or vice versa. We also observed smoke aerosols
29 during the case studies presented in Section 4, which were shown to have SSA values as low as
30 0.85 during ACE-Asia (Seinfeld et al., 2004). Thus, we expect similar errors (~3.8%) for
31 instances when our continental aerosol model is used to retrieve AOD in highly absorbing smoke

1 plumes. Note that for scenes involving pure dust plumes the RMS errors mentioned above are
2 more representative of lower bound error estimates due to unrealistic dust scattering properties
3 that can arise from the 6SV Mie-scattering calculations, which can lead to higher uncertainties
4 in AOD (Dubovik et al., 2002; Levy et al., 2007b).

5 5.4 NRT AOD composites

6 When generating our AOD composite product, uncertainties may arise from averaging
7 the individual GEO and LEO AOD retrievals onto a common grid (Section 3.6) due to
8 differences in their AOD retrievals, spatial resolution, observation times, and viewing geometry.
9 We expect minimal uncertainties with averaging the GEO AOD onto a common grid, since we
10 developed very similar retrievals algorithms for the GOES and MTSAT imagers that use the
11 same 6SV aerosol model and LUT approaches. In addition, there will only be a small number of
12 instances when both GOES and MTSAT AOD retrievals fall within the same grid box due to the
13 limited overlap between their geographical coverage. Conversely, when averaging the MODIS
14 and VIIRS AOD, significant uncertainties may arise due to the differences between their AOD
15 algorithms as discussed in Section 2.2. Fig. 9a-b shows an example of the MODIS Level 2 AOD
16 retrievals and VIIRS AOD retrievals for the 18 March 2014 case study presented in Section 4.1.
17 These LEO sensors show a very similar spatial distribution of AOD throughout the domain
18 where both retrieve $AOD > 1$ for the polluted dust plume extending northeast from eastern China
19 ($\sim 33^\circ\text{N}$, 120°E) to the Sea of Japan ($\sim 36^\circ\text{N}$, 135°E) and $AOD > 0.5$ throughout much of
20 Southeast Asia ($\sim 16^\circ\text{N}$, 100°E). The most significant difference between the LEO AOD
21 retrievals appear over the Korean peninsula ($\sim 38^\circ\text{N}$, 128°E) where MODIS and VIIRS AOD is
22 around 0.7 and 0.5, respectively. Both algorithms utilize their dust models to retrieve AOD in
23 this region, therefore, VIIRS is likely biased low due to the assumption of spherical dust particles
24 in the model. Nevertheless, the correlation between VIIRS and MODIS AOD throughout this
25 entire domain is very high ($R = 0.92$), which suggests that our approach of averaging VIIRS and
26 MODIS AOD to generate the AOD composite leads to a minimal uncertainties.

27 28 **6. Validation**

29 We validate our daily AOD composites using level 1.5 AERONET 550 nm AOD from 15
30 different sites across East Asia and 5 different sites across western United States during the 6 day
31 period (18-23 March 2014) of the trans-Pacific transport event presented in this paper. To

1 conduct a proper validation we calculated the average of the all available AERONET AOD
2 retrievals for each site during the 24 hour period of the daily AOD composites. Then, we use the
3 nearest neighbor approach to find the closest composite grid box to each AERONET site. Fig.
4 10a shows a high correlation ($R = 0.87$) between AERONET AOD and the daily AOD
5 composites including only LEO satellite retrievals. The slope of the linear regression line
6 indicates the high bias of about 0.10 in the LEO retrievals. Fig. 10b shows a slightly lower
7 correlation of $R = 0.79$ between AERONET AOD and our daily AOD composite product
8 including both LEO and GEO satellite retrievals, which is not surprising considering the higher
9 uncertainties associated with the GEO retrievals. However, the slope of the linear regression line
10 has decreased to near 1.0 as our daily AOD composite product is associated with a high bias of
11 only 0.024. Overall, this validation exercise has shown the improvement in AOD spatial
12 coverage from inclusion of the GEO retrievals in our AOD composite does not lead to a
13 significantly degraded product. Thus, our composite product can be used with confidence for
14 quantitatively tracking aerosol plumes.

15

16 **7. Conclusion**

17 The primary goal of this study was to generate a NRT daily AOD composite product that
18 combines GEO and LEO satellite observations to assist with monitoring and tracking the trans-
19 Pacific transport of aerosol plumes. In this paper, we present examples of the AOD composite
20 product for a case study of trans-Pacific transport of Asian aerosols in mid-March 2014.

21 Although the MODIS and VIIRS LEO satellites generally provide high-quality AOD retrievals
22 in cloud-free scenes (excluding the polar region), they only observe the same area once during
23 the daytime period, which increases the likelihood of cloud and sun glint contamination. This
24 can cause gaps in daily AOD coverage as shown by the case studies presented in this paper.

25 Thus, we take advantage of the high temporal resolution of the GOES-15 and MTSAT-2 GEO
26 satellites by developing AOD retrieval algorithms based on the continental and desert aerosol
27 models in the 6SV1.1 RTM. We also develop a unique cloud/dust detection algorithm utilizing
28 spectral, spatial, and temporal techniques to disregard cloud contaminated pixels and locate dust
29 pixels for the desert aerosol model. Overall, when merging the GEO and LEO retrievals, we
30 generated a daily AOD composite product that provided additional spatial coverage of AOD
31 across our domain from Asia to the North America. We showed that the coverage of aerosol

1 plumes propagating from Asia to the western Pacific were better captured by our AOD
2 composite product than the individual GEO and LEO products. Our AOD composite also
3 showed increased spatial coverage of AOD across the eastern Pacific, which can assist with
4 tracking the trans-Pacific transport of aerosols. Additionally, the incorporation of the 6SV desert
5 model into our AOD retrieval algorithms helped depict areas of dust plumes over the Gobi and
6 Taklamakan deserts that were not shown by the LEO products.

7 Although the AOD composite product showed an increase in spatial coverage of AOD
8 across our domain from Asia to North America, we noted several issues pertaining to the GEO
9 AOD retrievals. We showed that high biases in AOD can appear in the tropical Pacific due to
10 cloud artifacts impacting the GEO retrievals, which were more apparent over the tropical western
11 Pacific than over the tropical eastern Pacific. However, we also found that biases in AOD can
12 arise from the 28 day composite technique contained within the R_{sfc} retrieval procedure. The
13 variation in solar geometry during the 28 day composite technique can lead to uncertainties in
14 AOD of up to 34% over areas of minimal R_{sfc} such as the tropical Pacific. Conversely, we found
15 that the GEO AOD retrievals are generally biased low across the northern Pacific from cloud
16 artifacts impacting the R_{sfc} retrieval procedure. We did not discuss uncertainties in the GOES
17 AOD retrieval algorithm over land as we are mostly concerned with tracking the aerosol plumes
18 during their transport to the west coast of North America. Nevertheless, our assessment of the
19 GOES AOD retrieval algorithm over land showed that it performs adequately over the west coast
20 of the United States.

21 We did not show examples of the 6-hourly AOD composite product, since the daily
22 product is more pertinent for the focus of this paper where we track the trans-Pacific transport of
23 aerosols. Nevertheless, it is important to note that the GEO AOD retrievals have a greater
24 impact on this product, since LEO satellites have limited coverage across our domain during the
25 6 hour time window. Thus, the 6-hourly product can have important implications for aerosol
26 forecasting as the shorter time window is more appropriate for the AOD assimilation process.
27 Thus, the assimilation of both LEO and GEO satellite AOD retrievals can provide a more
28 comprehensive coverage of AOD into chemistry models (e.g., Weather Research and Forecasting
29 coupled with Chemistry (WRF-Chem)), which can help improve the representation of the
30 simulated aerosol fields. This can ultimately improve air quality forecasts and the simulation of
31 the aerosol-cloud-precipitation processes.

1 The future capability of GEO satellites for monitoring and tracking aerosol plumes will
2 be greatly enhanced with the upcoming launch of the next-generation NOAA GOES-R and
3 recently launched JMA Himawari satellites. These advanced GEO satellites perform full disk
4 scans every 5 minutes, and carry sensors consisting of 16 spectral bands with 0.5 km spatial
5 resolution at nadir for the 0.64 μm visible band with a spectral resolution from about 0.59 μm to
6 0.69 μm . Uncertainties associated with GEO AOD retrievals will be greatly reduced when using
7 GOES-R and Himawari measurements. Also, the much improved spatial resolution of these
8 satellites will help track aerosol plumes across the northern Pacific. This paper showed that
9 GOES-15 and MTSAT-2 do not have adequate spatial resolution to track aerosol plumes in the
10 northern parts of the Pacific. The very high temporal resolution of 5 minutes for the new
11 generation satellites will also lead to a more complete understanding of the aerosol spatial
12 distribution across the Pacific.

13

14 **Acknowledgements**

15 The MODIS Level 2 AOD products were downloaded from the Land, Atmosphere Near real-
16 time Capability for EOS (LANCE) system operated by the NASA/GSFC/Earth Science Data and
17 Information System (ESDIS) with funding provided by NASA/HQ. AOD from the VIIRS
18 aerosol Environmental Data Record was downloaded using the NOAA Comprehensive Large
19 Array-Data Stewardship System (CLASS) subscription service. The CALIPSO data was
20 obtained from the NASA Langley Research Center Atmospheric Science Data Center. The
21 authors gratefully acknowledge the NOAA Air Resources Laboratory (ARL) for the provision of
22 the HYSPLIT transport and dispersion model and READY website (<http://www.ready.noaa.gov>)
23 used in this publication. We would like to thank the anonymous reviewers who helped improve
24 the paper through their useful comments.

25

26

27

28

29

30

31

1 References

- 2 Ackerman, S. A.: Remote sensing aerosols using satellite infrared observations, *J. Geophys.*
3 *Res.*, 102, 17069–17079, 1997.
- 4 Ackerman, S., Strabala, K., Menzel, P., Frey, R., Moeller, C., Gumley, L., Baum, B., S. W.
5 Seemann, and H. Zhang: Discriminating clear-sky from cloud with MODIS: Algorithm
6 theoretical basis document (MOD35), version 5.0, NASA Goddard Space Flight Cent.,
7 Greenbelt, Md, 2006.
- 8 Al-Saadi, J., Szykman, J., Pierce, B. R., Kittaka, C., Neil, D., Chu, D. A., Remer, L., Gumley, L.,
9 Prins, E., Weinstock, L., MacDonald, C., Wayland, R., Dimmick, F., and Fishman, J.:
10 Improving national air quality forecasts with satellite aerosol observations, *Bull. Am.*
11 *Meteorol. Soc.*, 86(9), 1249-1261, doi: 10.1175/BAMS-86-9-1249, 2005.
- 12 Ault, A. P., Williams, C. R., White, A. B., Neiman, P. J., Creamean, J. M., Gaston, C. J., Ralph,
13 F. M., and Prather, K. A.: Detection of Asian dust in California orographic precipitation,
14 *J. Geophys. Res.*, 116, D16205, doi:10.1029/2010JD015351, 2011.
- 15 Benjamin, S. G., Weygandt, S. S., Brown, J. M., Hu, M., Alexander, C., Smirnova, T. G., Olson,
16 J. B., James, E., Dowell, D. C., Grell, G. A., Lin, H., Peckham, S. E., Smith, T. L.,
17 Moninger, W. R., Kenyon J., and Manikin, G. S.: A North American Hourly
18 Assimilation and Model Forecast Cycle: The Rapid Refresh, *Mon. Weather Rev.*, early
19 online release, doi: <http://dx.doi.org/10.1175/MWR-D-15-0242.1>, 2015.
- 20 Diner, D. J., Beckert, J. C., Bothwell, G. W., and Rodrigues, J. I.: Performance of the MISR
21 instrument during its first 20 months in Earth orbit, *IEEE Trans. Geosci. Remote Sens.*,
22 40, 1449–1466, 2002.
- 23 Dubovik, O., Smirnov, A., Holben, B. N., King, M. D., Kaufman, Y. J., Eck, T. F., and Slutsker,
24 I.: Accuracy assessments of aerosol optical properties retrieved from Aerosol Robotic
25 Network (AERONET) Sun and sky radiance measurements, *J. Geophys. Res.*, 105,
26 9791–9806, 2000.
- 27 Dubovik, O., Holben, B. N., Lapyonok, T., Sinyuk, A., Mishchenko, M. I., Yang, P., and
28 Slutsker, I.: Non-spherical aerosol retrieval method employing light scattering by
29 spheroids, *Geophys. Res. Lett.*, 29(10), doi:10.1029/2001GL014506, 2002.
- 30 Dubovik, O., Sinyuk, A., Lapyonok, T., Holben, B. N., Mishchenko, M., Yang, P., Eck, T. F.,
31 Volten, H., Munoz, O., Weihelmann, B., van der Zande, W. J., Leon, J.-F., Sokorin, M.,
32 and Slutsker, I.: Application of spheroid models to account for aerosol particle
33 nonsphericity in remote sensing of desert dust, *J. Geophys. Res.*, 11, D11208,
34 doi:10.1029/2005JD006619, 2006.
- 35 Eck, T. F., Holben, B. N., Reid, J. S., Dubovik, O., Smirnov, A., O'Neill, N. T., Slutsker, I., and
36 Kinne, S.: Wavelength dependence of the optical depth of biomass burning, urban, and
37 desert dust aerosols, *J. Geophys. Res.-Atmos.*, 104, 31333– 31349, 1999.
- 38 Gong, S. L., Zhang, X. Y., Zhao, T. L., Zhang, X. B., Barrie, L. A., McKendry, I. G., and Zhao,
39 C. S.: A simulated climatology of Asian dust aerosol and its trans-Pacific transport. Part
40 II: Interannual variability and climate connections, *J. Clim.*, 19, 104-122, 2006.
- 41 Green, M., Kondragunta, S., Ciren, P., and Xu, C.: Comparison of GOES and MODIS aerosol
42 optical depth (AOD) to aerosol robotic network (AERONET) AOD and IMPROVE
43 PM_{2.5} mass at Bondville, Illinois, *J. Air Waste Manag. Assoc.*, 59, 1082–1091, 2009.
- 44 Hillger, D., Kopp, T., Lee, T., Lindsey, D., Seaman, S., Miller, S., Solbrig, J., Kidder, S.,

1 Bachmeier, S., Jasmin, T., and Rink, T.: First-Light Imagery from Suomi NPP
2 VIIRS, *Bull. Amer. Meteor. Soc.*, 94, 1019–1029, 2013.

3 Holben, B. N., Eck, T. F., Slutsker, I., Tanfé, D., Buis, J. P., Setzer, A., Vermote, E., Reagan, J.
4 A., Kaufman, Y. J., Nakajima, T., Lavenu, F., Jankowiak, I., and Smirnov, A.:
5 AERONET - A federated instrument network and data archive for aerosol
6 characterization, *Remote Sens. Environ.*, 66, 1–16, 1998.

7 Hsu, N. C., Tsay, S.-C., King, M. D., and Herman, J. R.: Deep blue retrievals of Asian aerosol
8 properties during ACE-Asia, *IEEE T. Geosci. Remote*, 44, 3180–3195, 2006.

9 Huang, J., N. C. Hsu, S.-C. Tsay, M.-J. Jeong, B. N. Holben, T. A. Berkoff, and E. J.
10 Welton (2011), Susceptibility of aerosol optical thickness retrievals to thin cirrus
11 contamination during the BASE-ASIA campaign, *J. Geophys. Res.*, 116, D08214,
12 doi:[10.1029/2010JD014910](https://doi.org/10.1029/2010JD014910).

13 Ignatov, A. and Stowe, L.: Aerosol Retrievals from Individual AVHRR Channels. Part I:
14 Retrieval Algorithm and Transition from Dave to 6S Radiative Transfer Model, *J. Atmos.*
15 *Sci.*, 59, 313–334, 2002.

16 Jackson, J., Liu, H., Laszlo, I., Kondragunta, S., Remer, L. A., Huang, J., and Huang, H.-C.:
17 Suomi-NPP VIIRS Aerosol Algorithms and Data Products, *J. Geophys. Res.*, 118,
18 12673–12689, doi:10.1002/2013JD020449, 2013.

19 Jethva, H., Torres, O., Remer, L. A., and Bhartia, P. K.: A Color Ratio Method for Simultaneous
20 Retrieval of Aerosol and Cloud Optical Thickness of Above-Cloud Absorbing Aerosols
21 From Passive Sensors: Application to MODIS Measurements, *IEEE T. Geosci. Remote*,
22 51, 3862–3870, doi:10.1109/TGRS.2012.2230008, 2013.

23 Kahn, R. A., Gaitley, B. J., Martonchik, J. V., Diner, D. J., Crean, K. A., and Holben, B.:
24 Multiangle Imaging Spectroradiometer (MISR) global aerosol optical depth validation
25 based on 2 years of coincident Aerosol Robotic Network (AERONET) observations, *J.*
26 *Geophys. Res.*, 110, D10S04, doi:10.1029/2004JD004706, 2005.

27 Khain, A., Rosenfeld, D., and Pokrovsky, A., Aerosol impact on the dynamics and microphysics
28 of deep convective clouds, *Q. J. R. Meteorol. Soc.*, 131, 2639–2663, 2005.

29 Kim, J., Yoon, J. M., Ahn, M. H., Sohn, B. J., and Lim, H. S.: Retrieving aerosol optical depth
30 using visible and mid-IR channels from geostationary satellite, MTSAT-1R, *Int. J.*
31 *Remote Sens.*, 29, 6181–6192, 2007.

32 Knapp, K. R., Frouin, R., Kondragunta, S., and Prados, A. I.: Towards aerosol optical Depth
33 retrievals over land from GOES visible radiances: Determining surface reflectance, *Int. J.*
34 *Remote Sens.*, 26, 4097–4116, 2005.

35 Kotchenova, S. Y., Vermote, E. F., Matarrese, R. and Klemm Jr., F.: Validation of a vector
36 version of the 6S radiative transfer code for atmospheric correction of satellite data. Part
37 I: Path radiance, *Appl. Opt.*, 45, 6762–6774, 2006.

38 Kotchenova, S. Y. and Vermote, E. F.: Validation of a vector version of the 6S radiative transfer
39 code for atmospheric correction of satellite data. Part II: Homogeneous Lambertian and
40 anisotropic surfaces, *Appl. Opt.*, 46, 4455–4464, 2007.

41 Levy, R. C., Remer, L. A., Mattoo, S., Vermote, E. F., and Kaufman, Y. J.: Second-generation
42 operational algorithm: Retrieval of aerosol properties over land from inversion of
43 Moderate Resolution Imaging Spectroradiometer spectral reflectance, *J. Geophys. Res.*,
44 112, D13211, doi:10.1029/2006JD007811, 2007a.

45 Levy, R. C., Remer, L. A., and Dubovik, O.: Global aerosol optical properties and

1 application to Moderate Resolution Imaging Spectroradiometer aerosol retrieval over
2 land, *J. Geophys. Res.*, 112, D13210, doi:10.1029/2006JD007815, 2007b.

3 Levy, R. C., Remer, L. A., Kleidman, R. G., Mattoo, S., Ichoku, C., Kahn, R., and Eck, T. F.:
4 Global evaluation of the Collection 5 MODIS dark-target aerosol products over land,
5 *Atmos. Chem. Phys.*, 10, 10399–10420, doi:10.5194/acp-10-10399-2010, 2010.

6 Levy, R. C., Mattoo, S., Munchak, L. A., Remer, L. A., Sayer, A. M., Patadia, F., and Hsu, N.
7 C.: The Collection 6 MODIS aerosol products over land and ocean, *Atmos. Meas. Tech.*,
8 6, 2989-3034, doi:10.5194/amt-6-2989-2013, 2013.

9 Liu, H., Remer, L. A., Huang, J., Huang, H.-C., Kondragunta, S., Laszlo, I., Oo, M., and
10 Jackson, J. M.: Preliminary evaluation of S-NPP VIIRS aerosol optical thickness, *J.*
11 *Geophys. Res.*, 119, 3942–3962, 2014.

12 Mace, G. G., Zhang, Q., Vaughan, M., Marchand, R., Stephens, G., Trepte, C., and Winker, D.:
13 A description of hydrometer layer occurrence statistics derived from the first year of
14 merged Cloudsat and CALIPSO data, *J. Geophys. Res.*, 114, D00A26,
15 doi:10.1029/2007JD009755, 2009.

16 Mecikalski, J. R., MacKenzie Jr., W. M., König, M., and Muller, S.: Cloud-Top Properties of
17 Growing Cumulus prior to Convective Initiation as Measured by Meteosat Second
18 Generation. Part II: Use of Visible Reflectance, *J. Appl. Meteor. Climatol.*, 49, 2544–
19 2558, 2010.

20 Meyer, K., Platnick, S., and Zhang, Z.: Simultaneously inferring above-cloud absorbing
21 aerosol optical thickness and underlying liquid phase cloud optical and microphysical
22 properties using MODIS, *J. Geophys. Res.*, 120, 5524–5547. doi:
23 10.1002/2015JD023128, 2015.

24 Molod, A., Takacs, L., Suarez, M., Bacmeister, J., Song, I.-S., and Eichmann, A.: The GEOS-5
25 atmospheric general circulation model: Mean climate and development from MERRA to
26 Fortuna, *NASA Tech. Rep. NASA TM-2012-104606*, Vol. 28, 117 pp., 2012.

27 Naeger, A. R., Christopher, S. A., and Johnson, B. T.: Multiplatform analysis of the radiative
28 effects and heating rates for an intense dust storm on 21 June 2007, *J. Geophys. Res.*,
29 118, 9316–9329, 2013.

30 Naeger, A. R., Christopher, S. A., Ferrare, R., and Liu, Z.: A new technique using infrared
31 satellite measurements to improve the accuracy of the CALIPSO cloud-aerosol
32 discrimination method, *IEEE Trans. Geosci. Remote Sens.*, 51, 642–653, 2013.

33 Paciorek, C. J., Liu, Y., Macias, H. M., and Kondragunta, S.: Spatiotemporal associations
34 between GOES aerosol optical depth retrievals and ground-level PM_{2.5}, *Environ. Sci.*
35 *Technol.*, 42, 5800–5806, 2008.

36 Pope, C. A., Burnett, R. T., Thun, M. J., Calle, E. E., Krewski, D., Ito, K., and Thurston, G. D.:
37 Lung cancer, cardiopulmonary mortality, and long-term exposure to fine particulate air
38 pollution, *JAMA*, 287, 1132–1141, 2002.

39 Prados, A. I., Kondragunta, S., Ciren, P., and Knapp, K. R., GOES Aerosol/Smoke Product
40 (GASP) over North America: Comparisons to AERONET and MODIS observations, *J.*
41 *Geophys. Res.*, 112, D15201, doi:10.1029/2006JD007968, 2007.

42 Rienecker, M. M., Suarez, M. J., Todling, R., Bacmeister, J., Takacs, L., Liu, H.-C., Gu, W.,
43 Sienkiewicz, M., Koster, R. D., Gelaro, R., Stajner, I., and Nielsen, J. E.: The GEOS-5
44 data assimilation system – documentation of versions 5.0.1 and 5.1.0, and 5.2.0, *NASA*
45 *Tech. Rep. NASA/TM-2008-104606*, Vol. 27, 92 pp., 2008.

46 Remer, L. A., Kaufman, Y. J., Tanré, D., Mattoo, S., Chu, D. A., Martins, J. V., Li, R.-R.,

1 Ichoku, C., Levy, R. C., Kleidman, R. G., Eck, T. F., Vermote, E., and Holben, B. N.:
2 The MODIS Aerosol Algorithm, Products, and Validation, *J. Atmos. Sci.*, 62,
3 947–973, doi:10.1175/JAS3385.1, 2005.

4 Remer, L. A., Mattoo, S., Levy, R. C., and Munchak, L. A., MODIS 3 km aerosol product:
5 algorithm and global perspective, *Atmos. Meas. Tech.*, 6, 1829-1844, 2013.

6 Rolph, G. D.: Real-time Environmental Applications and Display sYstem (READY)
7 Website (<http://www.ready.noaa.gov>), NOAA Air Resources Laboratory, College Park,
8 MD, 2016.

9 Schmid, B., Michalsky, J., Halthore, R., Beauharnois, M., Harrison, L., Livingston, J., Russell, P.,
10 Holben, B., Eck, T., and Smirnov, A.: Comparison of aerosol optical depth from four
11 solar radiometers during the fall 1997 ARM intensive observation period, *Geophys. Res.*
12 *Let.*, 26, 2725–2728, 1999.

13 Seinfeld, J. H., Carmichael, G. R., Arimoto, R., Conant, W. C., Brechtel, F. J., Bates, T. S.,
14 Cahill, T. A., Clarke, A. D., Doherty, S. J., Flatau, P. J., Huebert, B. J., Kim, J.,
15 Markowicz, K. M., Quinn, P. K., Russell, L. M., Russell, P. B., Shimizu, A., Shinozuka,
16 Y., Song, C. H., Tang, Y. H., Uno, I., Vogelmann, A. M., Weber, R. J., Woo, J. H., and
17 Zhang, X. Y.: ACE-ASIA – Regional climatic and atmospheric chemical effects of Asian
18 dust and pollution, *Bull. Am. Meteorol. Soc.*, 85, 367–380, 2004.

19 Sokolik, I. N.: The spectral radiative signature of wind-blown mineral dust: Implications for
20 remote sensing in the thermal IR region, *Geophys. Res. Let.*, 29, 2154,
21 doi:10.1029/2002GL015910, 2002.

22 Streets, D. G., Yarber, K. F., Woo, J.-H., and Carmichael, G. R.: Biomass burning in Asia:
23 Annual and seasonal estimates and atmospheric emissions, *Global Biogeochem. Cy.*, 17,
24 1099, doi:10.1029/2003GB002040, 2003.

25 Talbot, R. W., Dibb, J. E., Lefer, B. L., Bradshaw, J. D., Sandholm, S. T., Blake, D. R., Blake,
26 N. J., Sachse, G. W., Collins Jr., J. E., Heikes, B. G., Merrill, J. T., Gregory, G. L.,
27 Anderson, B. E., Singh, H. B., Thornton, D. C., Bandy, A. R., and Pueschel, R. F.:
28 Chemical characteristics of continental outflow from Asia to the troposphere over the
29 western Pacific Ocean during February-March 1994: Results from PEM-West B, *J.*
30 *Geophys. Res.*, 102, 28255–28274, doi: 10.1029/96JD02340, 1997.

31 Torres, O., Jethva, H., and Bhartia, P. K.: Retrieval of Aerosol Optical Depth above Clouds from
32 OMI Observations: Sensitivity Analysis and Case Studies, *J. Atmos. Sci.*, 69, 1037–1053,
33 doi:10.1175/JAS-D-11-0130.1, 2012.

34 Vermote, E. F. and Kotchenova, S.: Atmospheric correction for the monitoring of land surfaces,
35 *J. Geophys. Res.*, 113, D23S90, doi:10.1029/2007JD009662, 2008.

36 Wilkening, K. E., Barrie, L. A., and Engle, M.: Transpacific air pollution, *Science*, 290, 65–67,
37 2000.

38 Winker, D. M., Pelon, J. R., and McCormick, M. P.: The CALIPSO mission: Spaceborne
39 lidar for observation of aerosols and clouds, in *Proc. SPIE*, 4893, 1–11, 2003.

40 Winker, D. M., Pelon, J., Coakley Jr., J. A., Ackerman, S. A., Charlson, R. J., Colarco, P. R.,
41 Flamant, P., Fu, Q., Hoff, R. M., Kittaka, C., Kubar, T. L., Le Treut, H., McCormick, M.
42 P., Mégie, G., Poole, L., Powell, K., Trepte, C., Vaughan, M. A., and Wielicki, B. A.:
43 The CALIPSO Mission: A Global 3D View of Aerosols and Clouds, *Bull. Amer. Meteor.*
44 *Soc.*, 91, 1211–1229, 2010.

45 Witek, M. L., Garay, M. J., Diner, D. J., and Smirnov, A.: Aerosol optical depths over oceans: A

1 view from MISR retrievals and collocated MAN and AERONET in situ observations, J.
2 Geophys. Res., 118, 12,620–12,633, 2013.

3 Yu, H., Remer, L. A., Chin, M., Bian, H., Tan, Q., Yuan, T., and Zhang, Y.: Aerosols
4 from overseas rival domestic emissions over North America, Science, 337, 566–569,
5 2012.

6 Zhang, J., Reid, J. S., and Holben, B. N.: An analysis of potential cloud artifacts in MODIS over
7 ocean aerosol optical thickness products, Geophys. Res. Lett., 32, L15803,
8 doi:10.1029/2005GL023254, 2005.

9 Zhao, T. L., Gong, S. L., Zhang, X. Y., Blanchet, J. P., McKendry, I. G., and Zhou, Z. J.: A
10 simulated climatology of Asian dust aerosol and its trans-Pacific transport. Part I: Mean
11 climate and validation, J. Clim., 19, 88-103, 2006.

12
13
14
15
16
17
18
19
20
21
22
23
24
25
26
27
28
29
30
31
32
33
34
35

1 **Figures**

2

3

Satellite Instrument	Latency (min)	Spectral Bands	Repeat Coverage	Swath width (km)	Local Equator Crossing Time	Spatial resolution (at nadir)	Visible bands for 550 nm AOD retrieval	AOD uncertainty
Aqua/Terra MODIS	90	36	1 to 2 days	2330	Aqua - 1030 Terra - 1330	10x10 km	Band 1: 620-670 nm Band 3: 459-479 nm	$\pm 0.03 \pm 0.05 * \text{AOD}$ over ocean
S-NPP VIIRS	420	22	daily	3000	1330	6x6 km	Band M5: 662-682 nm Band M3: 478-488 nm	See MODIS
GOES-15 Imager	30	5	30 minutes	N/A	N/A	4x4 km	Band 1: 533-709 nm	18-34%; lower uncertainty over water
MTSAT-2 Imager	30	5	30 minutes	N/A	N/A	5x5 km	Band 1: 540-816 nm	See GOES-15

Table 1. Summary of satellites instruments used in producing the NRT AOD product.

5

6

7

8

9

10

11

12

13

14

15

16

17

18

GOES-15 and (MTSAT-2)		
Imager Band	Center Wavelength (μm)	Spatial Resolution (km)
1	0.63 (0.675)	1 (1.25)
2	3.9 (3.75)	4 (5)
3	6.48 (6.75)	4 (5)
4	10.7 (10.8)	4 (5)
5	N/A (12.0)	N/A (5)
6	13.3 (N/A)	4 (N/A)

1 *Table 2. Center wavelength and spatial resolution of*
2 *spectral bands onboard GOES-15 and MTSAT-2. MTSAT-2*
3 *is denoted in red parenthesis. The GOES-15 imager carries*
4 *bands 1-4 and 6 while the MTSAT-2 imager carries bands*
5 *1-5.*

4
5
6
7
8
9
10
11
12
13
14
15

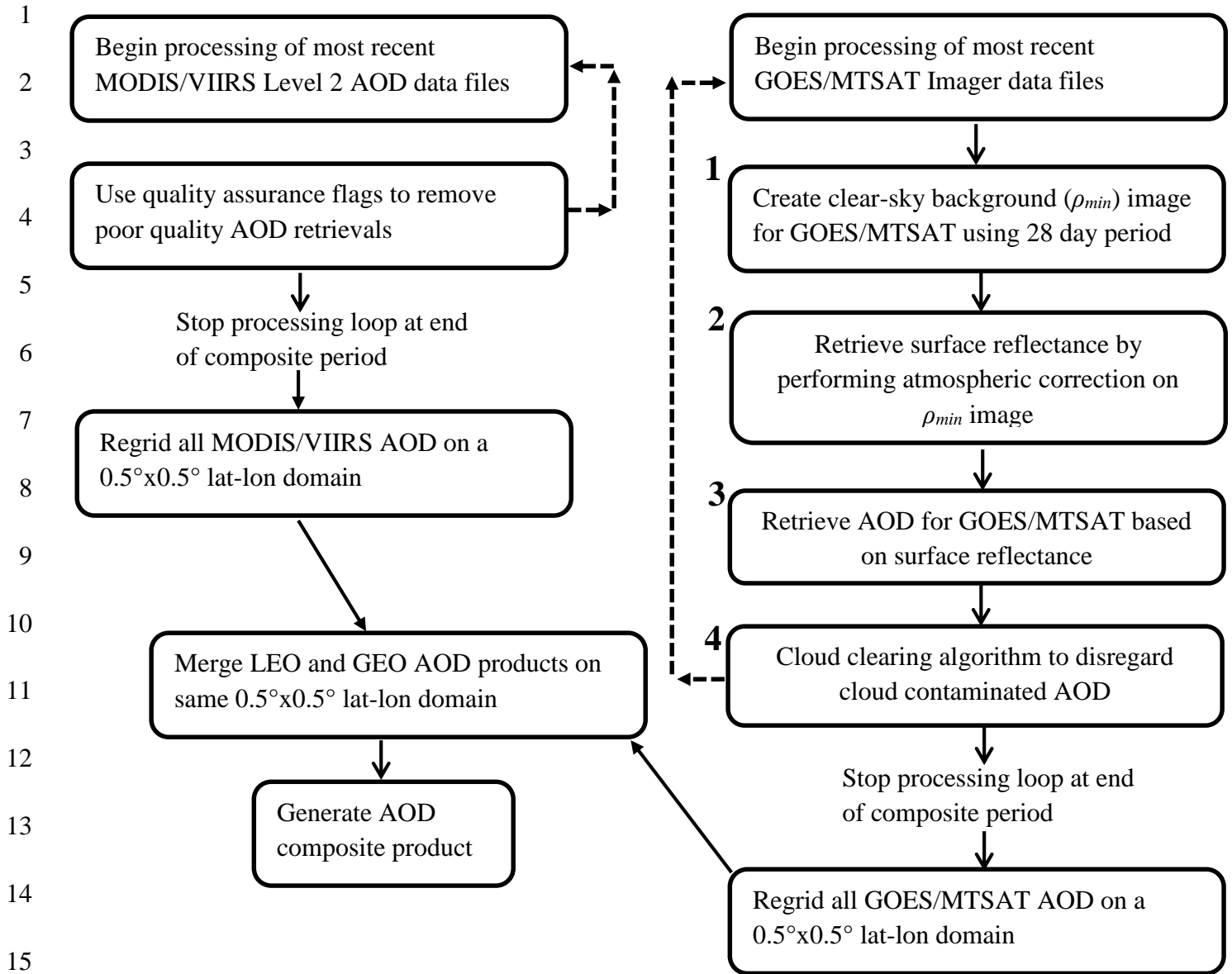


Figure 1. Schematic flow diagram of the steps involved in generating the NRT AOD composite product. The numbers 1-4 on the right-hand side of the schematic highlight the four major steps involved in the MTSAT/GOES AOD retrieval algorithms.

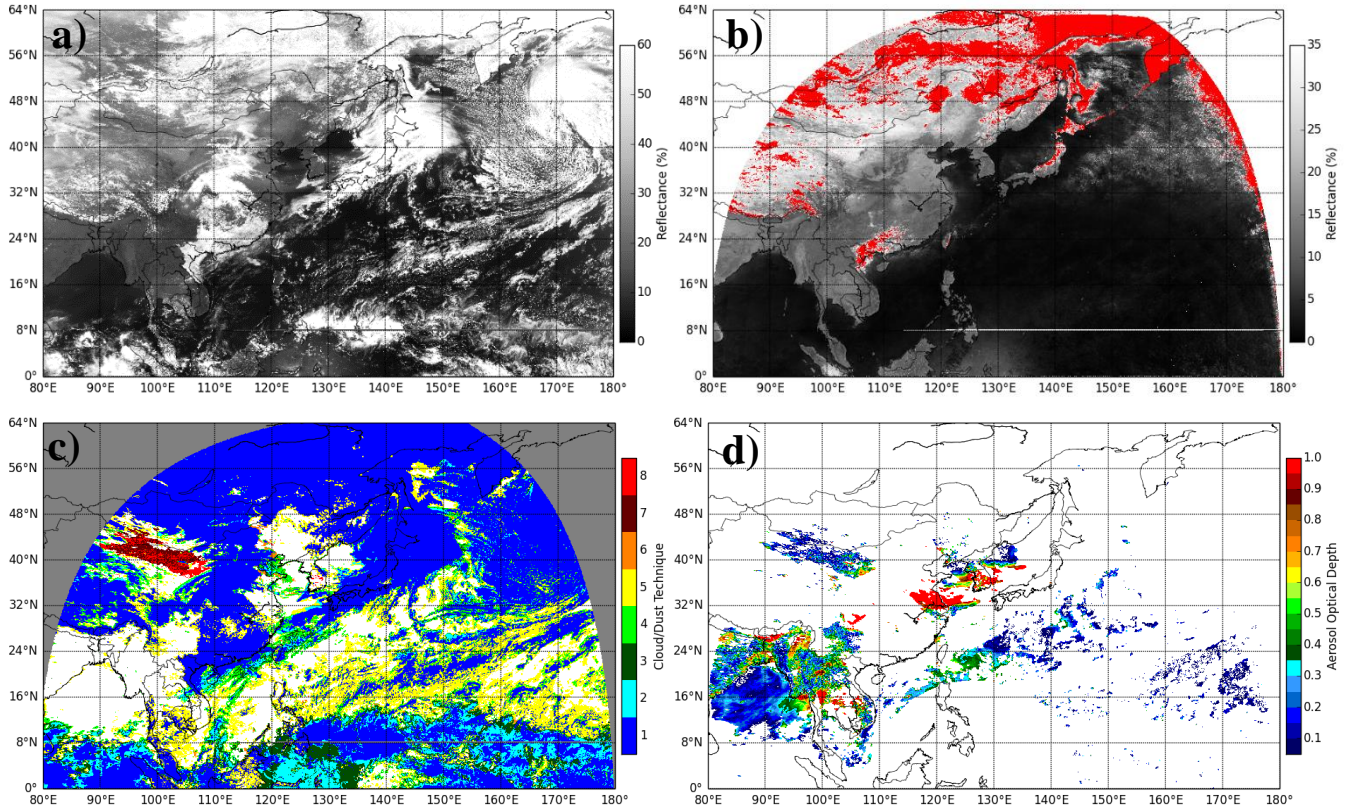


Figure 2. All panels pertain to 18 March 2014 at 0500 UTC. a) MTSAT-2 imager $0.68 \mu\text{m}$ reflectance scan. b) R_{sfc} retrievals for each valid pixel in MTSAT-2 imager scan where pixels having $R_{sfc} > 35\%$ are denoted in red. c) Cloud/dust detection results where the colorbar labels relate to technique # in Table 3. d) MTSAT AOD retrievals.

- 1
- 2
- 3
- 4
- 5
- 6
- 7
- 8
- 9

MTSAT cloud/dust detection algorithm		
Techniques	Condition	#
Spectral Techniques		
3.8 - 0.68 μm < -20%	Land/Water	1
3.8 - 12.0 μm > 25 K	Land	2
3.8 - 12.0 μm > 12 K	Water	2
10.8 - 12.0 μm > 2.0 K and 3.8 - 10.8 μm > 2.0 K	Water	3
Spatial Techniques		
3x3 σ 10.8 μm > 4.0 K or 3x3 σ 12.0 μm > 4.0 K	Land	4
3x3 σ 10.8 μm > 1.0 K or 3x3 σ 12.0 μm > 1.0 K	Water	4
3x3 σ 0.68 μm > 3.0% or 5x5 σ 0.68 μm > 3.0%	Land	5
3x3 σ 0.68 μm > 1.5% or 5x5 σ 0.68 μm > 1.5%	Water	5
Temporal Techniques		
10.8 μm_{time} > 3.0 K or 12.0 μm_{time} > 3.0 K	Water	6
10.8 μm_{time} > 10.0 K and 12.0 $\mu\text{m}_{time}/10.8 \mu\text{m}_{time}$ > 1.0 K	Land	6
Dust Techniques		
10.8 - 12.0 μm < -1.0 K	Cloud	7
3x3 σ 0.68 μm < 4.0% & 5x5 σ 0.68 μm < 4.0%	Cloud	7
3.8 - 10.8 μm > 4.0 K	Cloud	7
12.0 μm > 258 K	Cloud	7
10.8 - 12.0 μm <= -0.5 K or Rsfc > 20%	Cloud-free	8

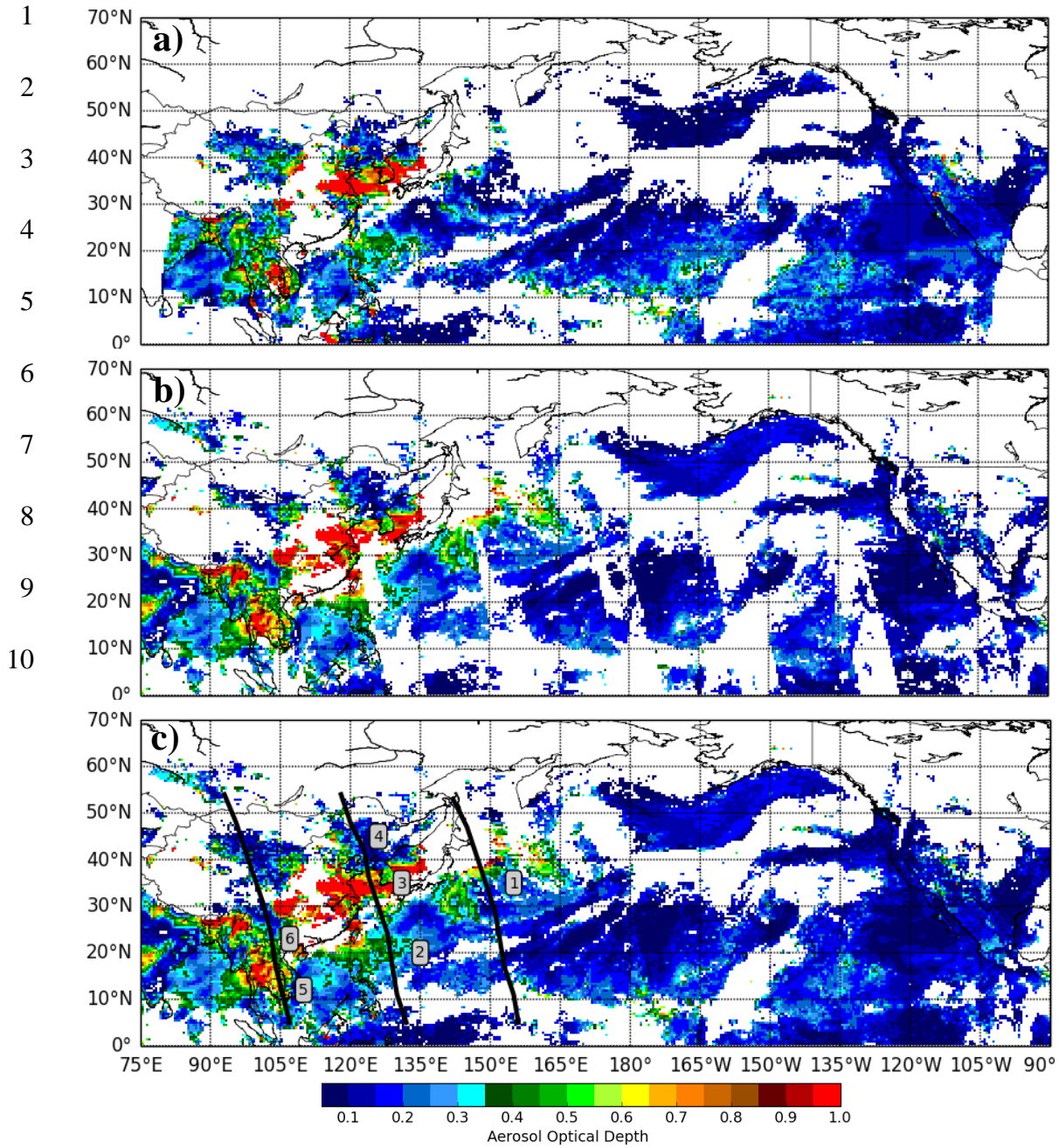
1 *Table 3. MTSAT cloud clearing algorithm with the various techniques and thresholds in*
2 *the left column, center column shows the conditions when the techniques are used, and*
3 *technique # relating to cloud/dust detection algorithm results in Figure 2c are in the*
4 *right column. The “time” subscript indicates a temporal technique.*

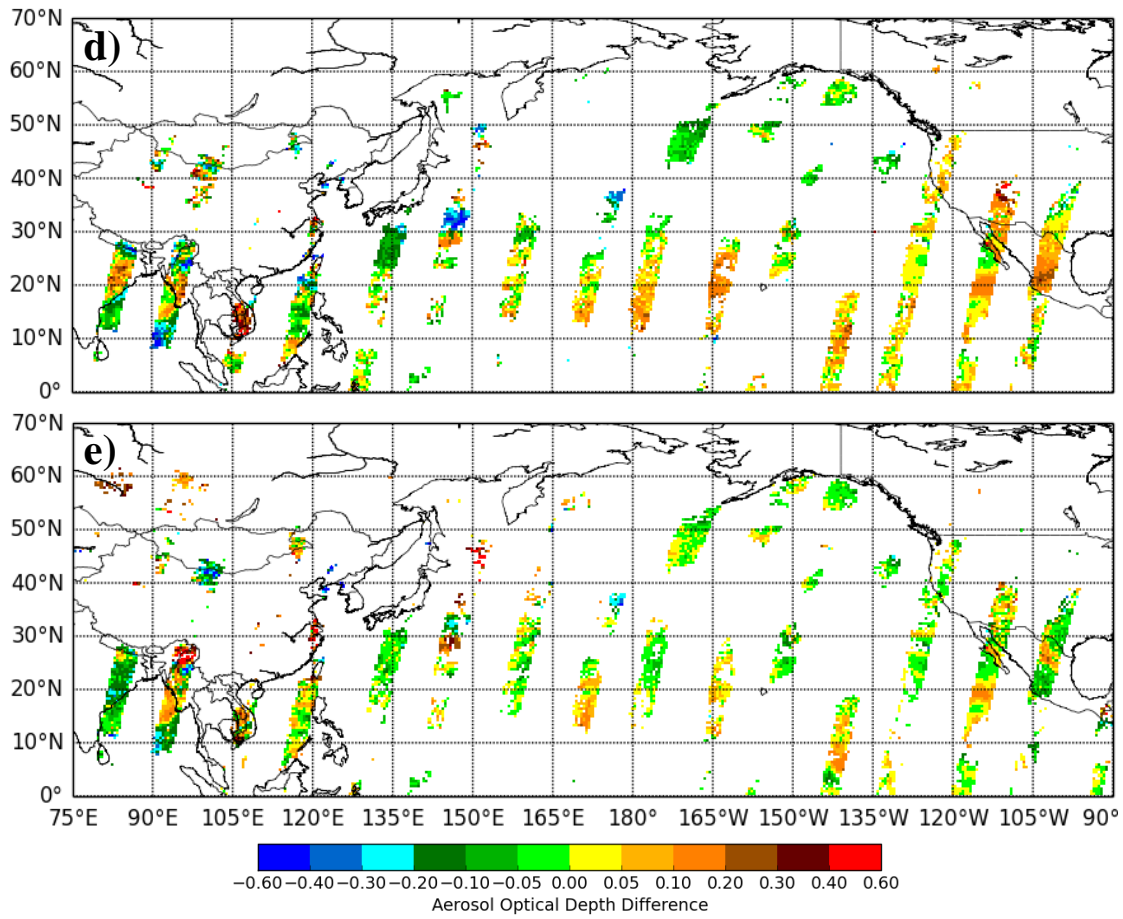
3

4

5

6





- 1
- 2
- 3
- 4
- 5
- 6
- 7
- 8
- 9
- 10

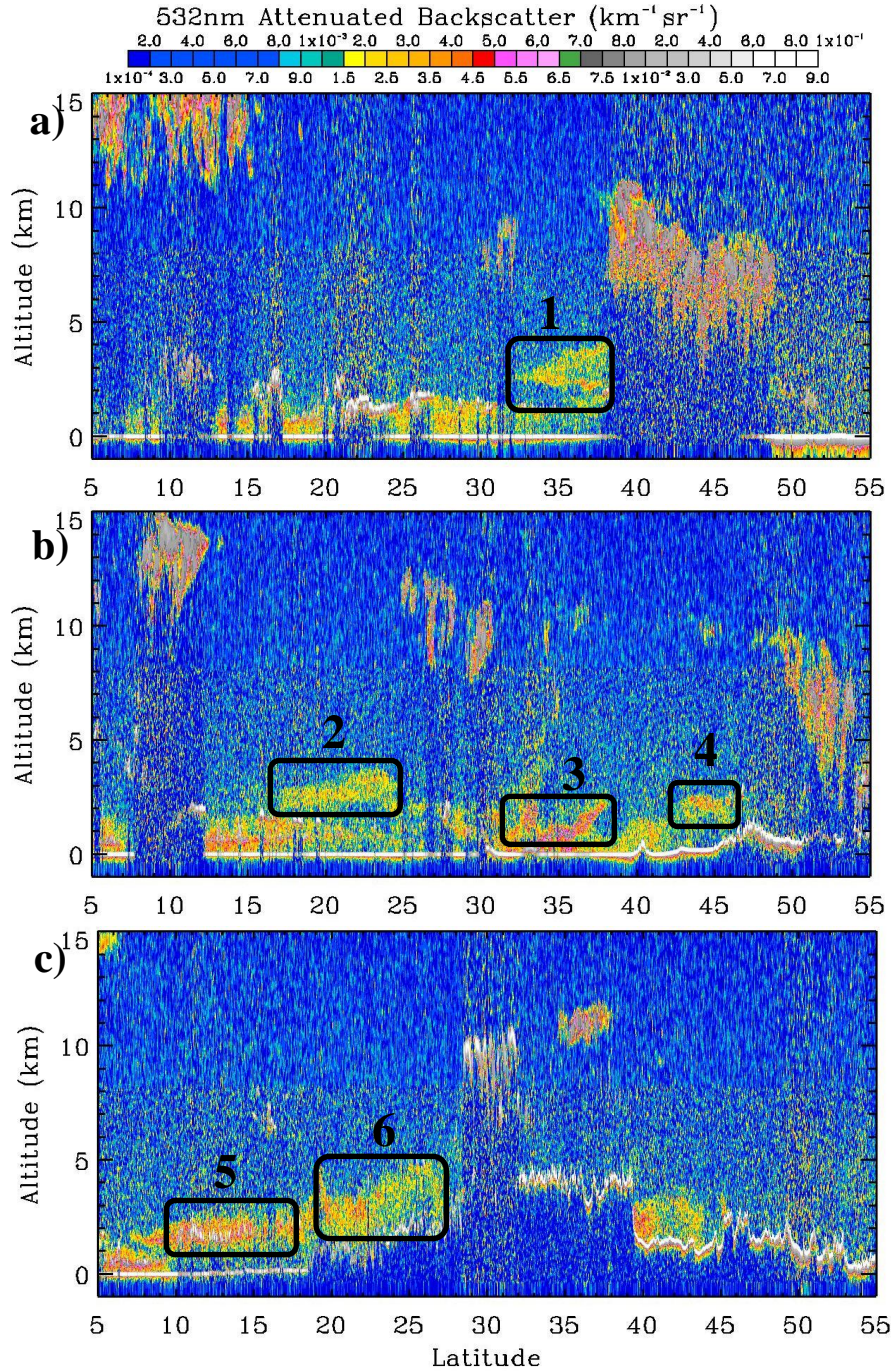
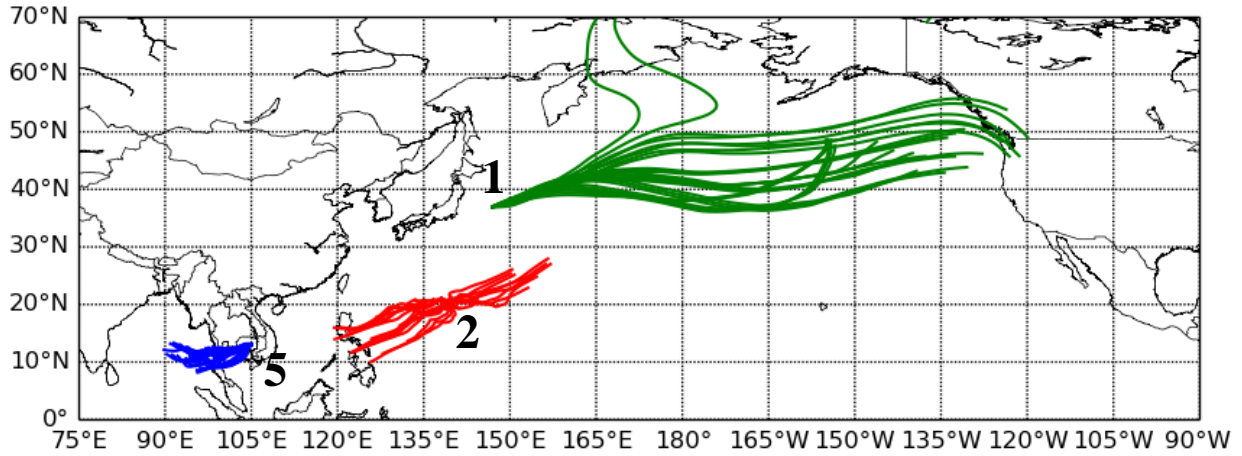


Figure 4. All panels show CALIPSO 532 nm attenuated backscatter profiles on 18 March 2014. CALIPSO transects are indicated in Figure 4c (black lines), which are increasing in time from east to west with a) at about 0320 UTC, b) at about 0500 UTC, and c) at about 0640 UTC. Boxes highlight regions of interest. The location of these boxes along the CALIPSO transects are also indicated in Figure 4c.

1

2



3

Figure 5. NOAA HYSPLIT model forward trajectory results for 4 day time period beginning 18 March 2014 at 0500 UTC. We initialize the model from locations 1,2, and 5 along the the CALIPSO transects in Figure 5. CALIPSO aerosol height information at these locations are also used to initialize the model.

4

5

6

7

8

9

10

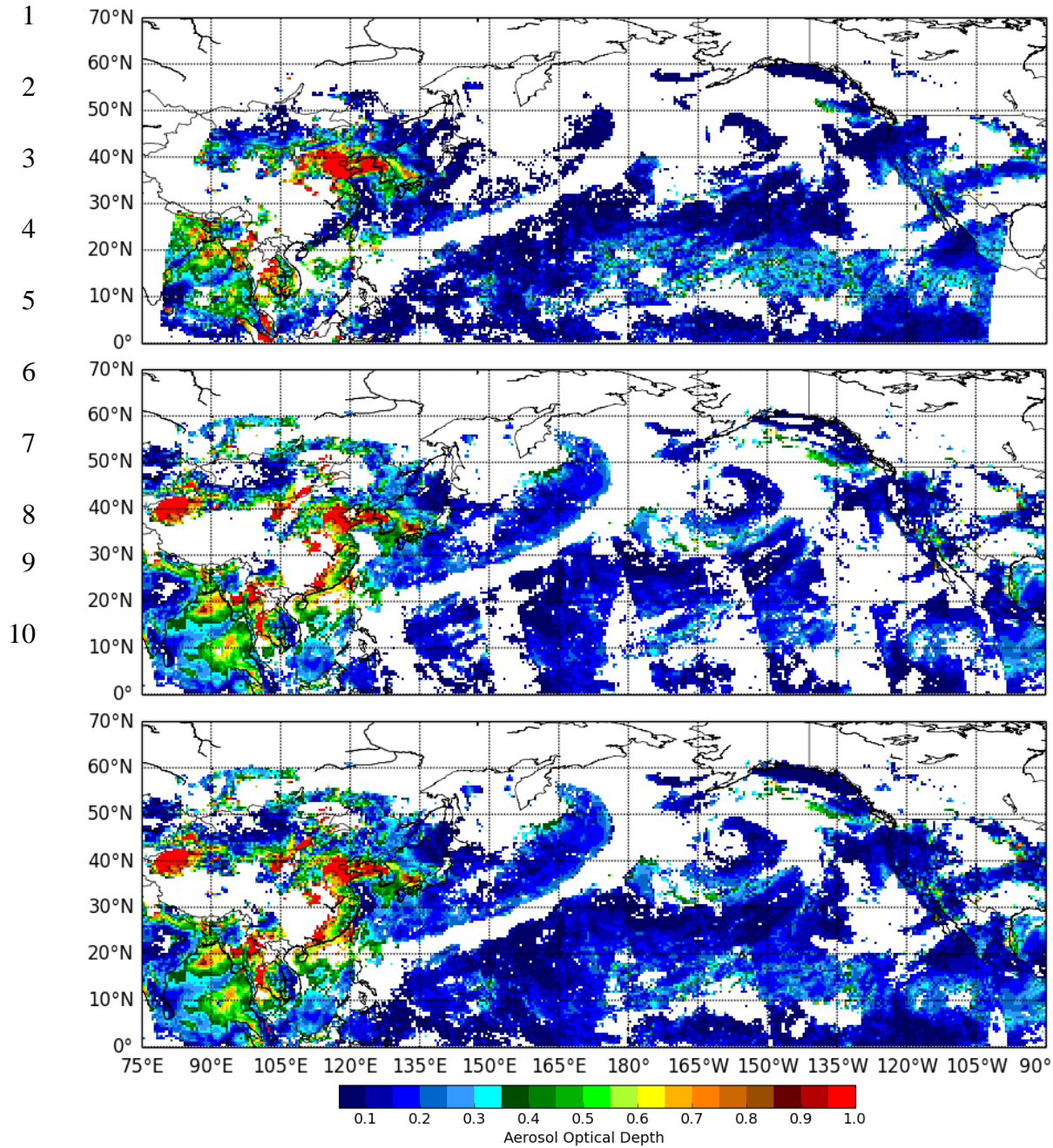
11

12

13

14

15



11 *Figure 6. Panels show the daily AOD composites with central time at 0000 UTC on 23*
 12 *March 2014. a) Example of the daily AOD composite when only MTSAT/GOES*
 13 *retrievals are utilized, b) example of when only MODIS/VIIRS retrievals are utilized, c)*
 14 *final version of our daily AOD composite product.*

13

14

15

Case	LEO coverage (# pixels / %)	GEO coverage (# pixels / %)	COMP coverage (# pixels / %)
18-Mar	48368 / 69	43906 / 62	58564 / 83
19-Mar	49980 / 71	45023 / 64	60050 / 85
20-Mar	46543 / 66	41348 / 59	55792 / 79
21-Mar	50071 / 71	44998 / 64	61755 / 88
22-Mar	43851 / 62	39004 / 55	52095 / 74
23-Mar	44960 / 64	40540 / 58	53580 / 76
Average	47296 / 67	42470 / 60	56973 / 81

Table 4. The coverage for the daily AOD composite maps when only LEO (MODIS/VIIRS) and GEO (MTSAT/GOES) sensors are considered compared to when both LEO and GEO sensors are considered (COMP) in our final product. We present the coverage statistics for six days including the 18 and 23 March case studies analyzed in this paper. The number of valid AOD retrievals across our AOD composite domain along with the percent coverage based on the total number of available grid boxes are shown.

1
2
3
4
5
6
7
8
9
10
11
12

1

	Location	θ_0 (°)	θ (°)	R_{sfc} (%)
Tropical	10°N, 100°E	21	42	10
Midlatitude	40°N, 130°E	42	46	5
Subarctic	55°N, 110°E	54	62	15

2 *Table 5. Location of GFS profiles used to estimate the uncertainty*
 3 *associated with U.S. standard profiles in the 6SV code4.*

3

4

5

6

7

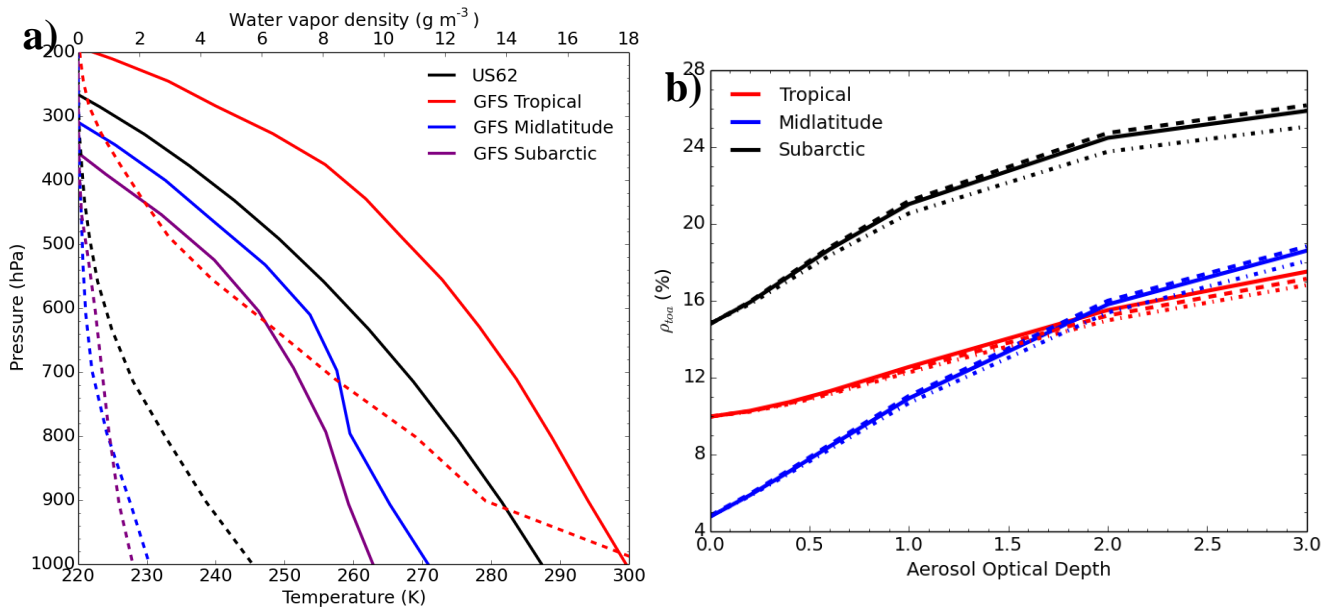
8

9

10

11

12



13 *Figure 7. a) Temperature (solid) and water vapor density (dashed) from the U.S. standard profile and GFS*
 14 *profiles extracted from tropical, midlatitude, and subarctic regions. b) 6SV model output of ρ_{10a} for AOD*
 15 *ranging from 0 to 3 for U.S. standard (solid) and GFS atmospheric profiles from January (dashed) and July*
 16 *(dot-dashed) 2014 in different regions. Specified θ_0 , θ , and R_{sfc} in Table 5 were additional inputs into the*
 17 *model.*

15

16

17

18

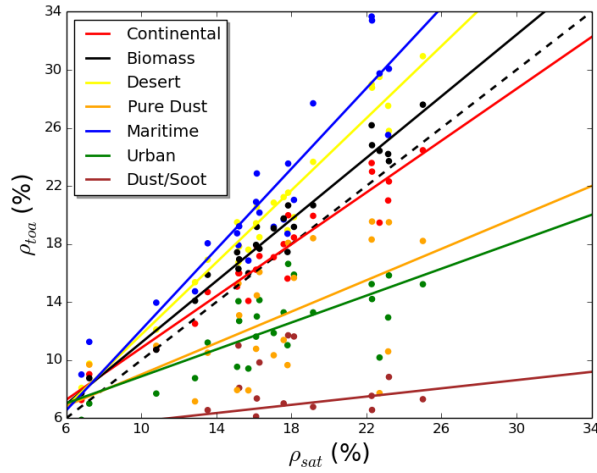
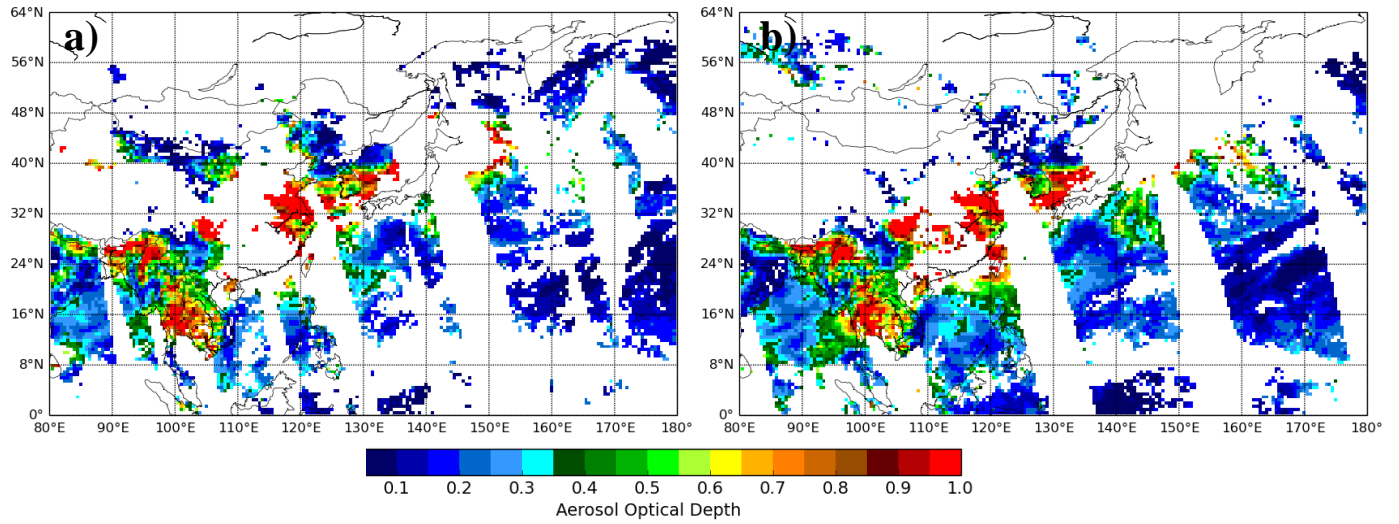


Figure 8. Observed ρ_{sat} versus 6SV ρ_{toa} results for 24 unique non-desert cases over eastern Asia during March and April 2014 where seven different aerosol models were tested for each case. Dust and pollution were the primary aerosol constituents during this period.

6SV Aerosol	SSA	$\rho_{sat} (\%) - \rho_{toa} (\%)$	RMS error (%)
Desert	0.95	-3.45	3.84
Urban	0.69	4.86	5.79
Continental	0.9	-0.09	1.31
Maritime	0.99	-4.79	5.7
Biomass	0.94	-1.63	1.9
Pure Dust	0.72	4.19	5.84
Dust/Soot	0.25	10.2	11.17

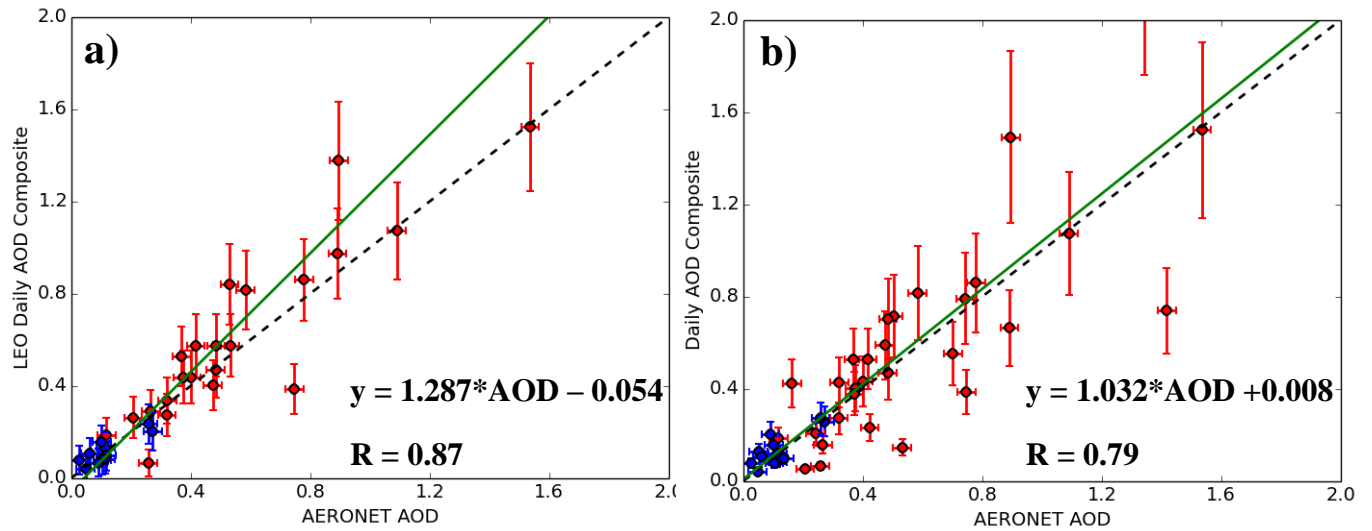
Table 6. Average difference between observed ρ_{sat} and 6SV ρ_{toa} for the 24 cases along with RMS error for each 6SV aerosol model. SSA at 500 nm is also shown for each aerosol model.



1 *Figure 9. a) MODIS Level 2 AOD retrievals and b) VIIRS AOD retrievals for the 18 March 2014*
 2 *case study presented in Section 4.1. The MODIS and VIIRS AOD retrievals are regridded onto*
 3 *identical domains for comparison purposes.*

4
5
6
7
8
9
10
11
12
13

1



2

3

4

5

6

*Figure 10. a) Daily average of level 1.5 AERONET 550 nm AOD retrievals versus the daily AOD composite including only LEO satellite retrievals for the six day period from 18-23 March 2014 (Table 4). b) Same as a) except daily average of AERONET AOD retrievals versus our daily AOD composite product (GEO and LEO retrievals). AERONET AOD from 15 different sites across East Asia (red) and 5 different sites across western United States (blue) were used to validate the daily AOD composites. Error bars are based on ± 0.015 uncertainty for AERONET AOD retrievals, $\pm 0.05 \pm 0.15 * AOD$ for LEO retrievals, and 25% uncertainty for our daily AOD composite product. The 25% uncertainty is the average of the GEO uncertainty range (18-34%). The linear regression lines are in solid green with corresponding equations and correlation coefficients in the lower right corner.*

7

8

9

10

11

12